

Nickel Oxide for Perovskite Photovoltaic Cells

Hansol Park, Rajneesh Chaurasiya, Bum Ho Jeong, Perumal Sakthivel,
and Hui Joon Park*

Organic–inorganic perovskite solar cells (PSCs) have shown tremendous progress from 3.8% power conversion efficiency (PCE) in 2003 to 25.2% in 2020 because of their wide range of light absorption, fast charge separation, long carrier diffusion length, and long carrier lifetime. The optoelectronic characteristics of hole transport material (HTM) and electron transport material (ETM) strongly affect photovoltaic (PV) performance and stability of PSCs. Recently, various inorganic HTMs with high efficiency, stability, and cost-effectiveness have been investigated. Among them, nickel oxide (NiO_x) is one of the most studied inorganic HTMs in terms of device performance and stability because it has high hole mobility, electrical conductivity, transmittance, and energetically favorable band alignment, along with environmental stability. This article overviews the recent progress on NiO_x -based planar PSCs. The main focus is on the structural, electrical and optical properties of the NiO_x thin film, which mainly depends on the synthesis methods and post-treatments. Firstly, a variety of methods are investigated to fabricate dense, compact and high crystallized NiO_x thin film. Moreover, multifarious doping strategies and surface functionalization using organic materials are summarized as approaches to improve their properties for realizing high performance p–i–n planar PSC devices.

regular usage of fossil fuels, it has been dwindling. To address these issues, extremely urgent efforts are being mobilized to identify the potential alternate energy sources that should be renewable, ecofriendly, and inexpensive. Solar energy represents one of the most abundant renewable energy sources, available to the human being. Indeed, 1 h of solar flux arriving to our planet is just enough for global energy consumption over a year.^[2] However, the contemporary challenges are to identify the viable systems for harvesting, transporting, and storing the solar energy in an efficient manner. The current photovoltaic (PV) electricity generation is completely dominated by the crystalline silicon solar cell due to its fairly high power conversion efficiency (PCE) of >26% with reasonable manufacturing cost.^[3] However, its rigidity, originated from its indirect bandgap, limits its utilization except in solar power plants and rooftop PV systems. As alternatives, the second-generation solar cells such as CdTe and

CIGS solar cells have been developed,^[4] and more importantly, third-generation solar cells like organic PVs, dye-sensitized solar cells (DSSCs), and quantum dot PV cells that can be fabricated by simple process techniques on low-cost unconventional substrates have shown tremendous advancement in their reproducibility and stability.^[5] However, their PCEs are still lagging behind the conventional silicon solar cells.


In this situation, the advent of perovskite solar cells (PSCs) in 2009 has revolutionized the third-generation solar cells due to its spectacular improvement in efficiency from 3.9% to 25% in a decade,^[6] along with its ease of fabrication methods that can be extended to a low-cost roll-roll process. In general, the organic–inorganic mixed-halide perovskites ABX_3 (A site: methyl ammonium (CH_3NH_3^+) or formamidinium ($\text{CH}_3(\text{NH}_2)_2^+$) with a mixture of Cs^+ or Rb^+ , B site: Pb^{2+} or Sn^{2+} , and X site: Cl^- , Br^- , or I^-) have been utilized as photoactive light absorbers due to their excellent optoelectronic properties such as high light absorption coefficient (10^5 cm^{-1}), small exciton binding energy, convenient bandgap tunability, large charge carrier diffusion length (>1 μm), and fairly high defects tolerance capacity.^[7] In addition to these these superior optoelectronic properties, perovskites have good flexibility in the design of device architecture and configuration. In general, PSCs can be classified into two basic structures, as regular (n–i–p) and inverted (p–i–n) structures, which depend on the position of electron transport layer (ETL) and

1. Introduction

With a rapid increase in population and industrialization, annual energy consumption is predicted to be about 30 TW in 2050, which is almost double compared with the consumption of 2015.^[1] Although the usage of fossil fuel has propelled our welfare and quality of life as a primary energy source, it exacts a huge penalty on humankind as well as the environment. Due to

H. Park, Dr. R. Chaurasiya, B. H. Jeong, Dr. P. Sakthivel, Prof. H. J. Park
Department of Organic and Nano Engineering
Hanyang University
Seoul 04763, Republic of Korea
E-mail: huijoon@hanyang.ac.kr

H. Park, B. H. Jeong, Prof. H. J. Park
Human-Tech Convergence Program
Hanyang University
Seoul 04763, Republic of Korea

 The ORCID identification number(s) for the author(s) of this article can be found under <https://doi.org/10.1002/adpr.202000178>.

© 2021 The Authors. Advanced Photonics Research published by Wiley-VCH GmbH. This is an open access article under the terms of the Creative Commons Attribution License, which permits use, distribution and reproduction in any medium, provided the original work is properly cited.

DOI: 10.1002/adpr.202000178

hole transport layer (HTL) on the exterior portion of the cell confronted by incident light first.^[8] Further, it can be also divided into two categories, mesoporous and planar structures. In the mesoporous PSCs, the mesoporous TiO₂ scaffold layer is usually incorporated between the perovskite and ETL layer,^[9] which is analogous to the solid-state DSSCs. The high PCE of 25.5% with a regular architecture was attained, in which mesoporous TiO₂ acted as the ETL.^[6] However, the mesoporous ETL requires high-temperature annealing, which restricts the compatibility with flexible and tandem PSC applications. Moreover, the mesoporous layer with a thickness greater than 150 nm showed ineffective electron transport property due its high surface roughness.^[10] As such, it is ideal to fabricate thin mesoporous ETLs although this is challenging. These limitations led to the emergence of the simplified planar configurations of PSCs (planar n-i-p and p-i-n).

As a general tendency, the regular-type (n-i-p) PSCs, which use crystalline ETLs (TiO₂, SnO₂, ZnO, etc.), have shown high efficiency compared with that of inverted-type (p-i-n) PSCs, and the superior stability of those ETLs provides a large process window to the following solution-based perovskite layer formation (e.g., solvent, processing temperature, etc.).^[11] Nevertheless, inverted-type PSCs, which resemble the structures of organic PV cells, are also under the spotlight, due to their advantages such as low-temperature processibility suitable for the processing of flexible devices.^[12] It has been widely known that ETL and HTL play a crucial role to achieve better performance in PSCs, and various efforts have been conducted to modify the ETL and HTL.^[13–16] As for the ETL, various types of stable inorganic semiconductors are available, but, most hole transport materials (HTM) have an organic nature, are less stable as they are easily degraded by water and oxygen, and reduce device stability as well as efficiency. Hence, there is an urgent need to develop more efficient inorganic HTMs.

The ideal HTM should possess the following characteristics such as 1) better energy-level alignment with perovskite (i.e., highest occupied molecular orbital (HOMO) level of HTM is well matched with the valence band of the perovskite), which promotes the extraction of holes from the perovskite and reduces their recombination at the interface, 2) high hole mobility, which facilitates the transportation of hole carriers, 3) high chemical and thermal stability, and 4) facile processibility with low production cost and a simple preparation procedure, which are more applicable to future large-scale applications.^[17] The varieties of organic materials have been developed as HTMs in n-i-p and p-i-n configurations of PSCs. Among these, the small-molecule-based 2, 2', 7, 7'-tetrakis (N,N-di-p-methoxyphenylamine)-9, 9'-spirobifluorene (spiro-OMeTAD) has been one of the most widely used HTMs so far, which exhibited a PCE over 23% in planar PSCs.^[18] However, low hole mobility, amorphous nature, and tedious synthesis procedure additionally require p-type dopants (i.e., FK209), and high cost limits its further usage. In contrast, the organic polymer-based poly(3,4-ethylenedioxythiophene):poly(4-styrenesulfonate) (PEDOT:PSS) has been also widely used as a HTM in inverted PSCs.^[19] However, its work function, unmatched with the valence band of perovskite, poor stability, and high preparation cost constrain its further extension to a large-scale practical application. Therefore, considerable research activities in this field have been

dedicated to the exploration of alternative low-cost and efficient inorganic HTMs in PSCs.^[20]

So far, various inorganic HTMs such as CuSCN, CuI, Cu₂O, CuS, CuGaO₂, CuAlO₂, NiO_x, MoO_x, and MoS₂ have been used as HTLs in PSCs.^[21–30] Among these, NiO_x is one of the most promising low-cost HTMs. Nickel oxide has a cubic structure with *Fm3m* space group similar to NaCl, and the corresponding lattice parameter is 0.4173 nm. Pure stoichiometric NiO behaves as an insulator at room temperature and its electrical conductivity is just less than 10⁻¹¹ S cm⁻¹.^[31] However, due to the presence of NiOOH and Ni₂O₃, excess amount of oxygen is always observed in practice, and those induce the nonstoichiometric state, represented as NiO_x. Excess amount of oxygen leads to Ni vacancies and thus holes are created, which provide a p-type characteristic to NiO_x.^[32] Optoelectronic properties of NiO_x are highly sensible with the Ni and O stoichiometry, and this can be tuned by processing conditions. For example, it has been reported that the stoichiometry of the as-deposited film, to be NiO_{1.96 ± 0.10}, ensuring around 90% of Ni(OH)₂ along with 10% of NiO, can be changed to be NiO_{1.07 ± 0.16} and NiO_{1.17 ± 0.12} at 200 and 400 °C, respectively.^[33] A nonstoichiometric NiO_x film, synthesized by a chemical precipitation method, showed an atomic ratio of Ni:O to be 1:1.14, in which NiOOH, Ni₂O₃, and NiO coexisted with 1.13:1.22:1 ratio, and its composition and its related work function, affecting the performances of solar cells, were shown to be changed over 200 °C annealing temperature.^[34]

NiO_x has numerous merits, including excellent visible transparency with a wide bandgap (>3.5 eV), a deep lying valence band maximum (VBM) (*E*_{VBM}: 5.2 eV), superior chemical, thermal, and light stability, and compatibility with low-temperature processes, feasible for flexible substrates.^[35] The p-i-n PSCs, built on various types of NiO_x layers (e.g., solution-based processes and vacuum-assisted depositions), have shown promising performances with negligible hysteresis and long-term stability.^[36–38] However, their low intrinsic conductivity (≈10⁻⁴ S cm⁻¹) and their surface defects, which were especially pin holes and island morphology, have been long-standing issues to resolve.^[31] Furthermore, a relatively distinct energy gap between their Fermi level and VBM can induce a large energy-level offset at the interface between NiO_x and perovskite.^[39–46] In this Review, we will discuss the strategies to overcome these drawbacks by enhancing their properties, including their synthetic routes, extrinsic doping processes, and modifications for defect passivation. Finally, the challenges and future outlooks for further improving the performance and stability of NiO_x-based PSCs will be discussed.

2. Synthetic Methods of NiO_x

Energy bands of HTMs for PSC devices are shown in **Figure 1**, for reference. Among those, the approaches, based on NiO_x and its derivatives, for p-i-n-structured PSCs, are main the focus of this Review. The properties of NiO_x thin films are largely affected by their synthetic methods including process conditions, because every synthesis method provides different concentrations of Ni³⁺ and Ni²⁺ valence states on the thin film, and its morphology can be significantly affected by the methods. These properties lead to the variation of PV performances of PSCs. In this section, we

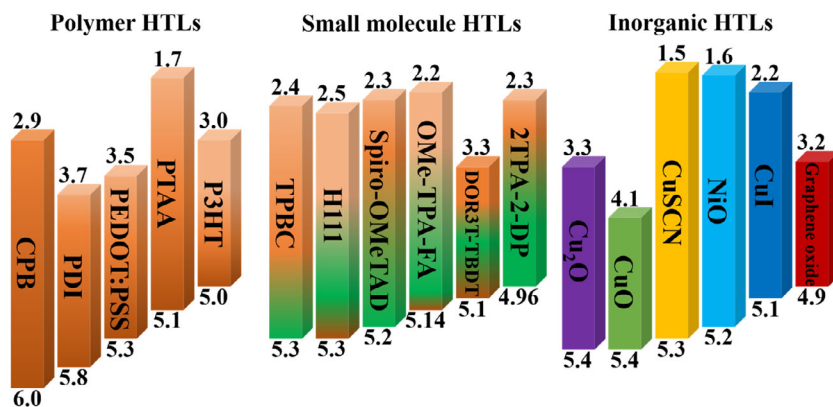


Figure 1. Energy bands of HTLs used for PSC applications.^[32]

summarize those methods, developed to synthesize high-quality NiO_x thin film (**Figure 2**), and their impacts on the film properties and PV performance are discussed.

2.1. Solvothermal Synthesis

The solvothermal method has been widely utilized for the synthesis of NiO_x nanocrystals. This method has easy processibility, and the distribution of particle size and shape including its crystallinity can be precisely controlled. NiO_x nanoparticles (NPs), synthesized by this method, are already in the crystalline form, and therefore the high-temperature annealing process can be often skipped after spin casting,^[47,48] but low-temperature post-annealing is usually required to remove the residual organic solvent, remaining on the surface.

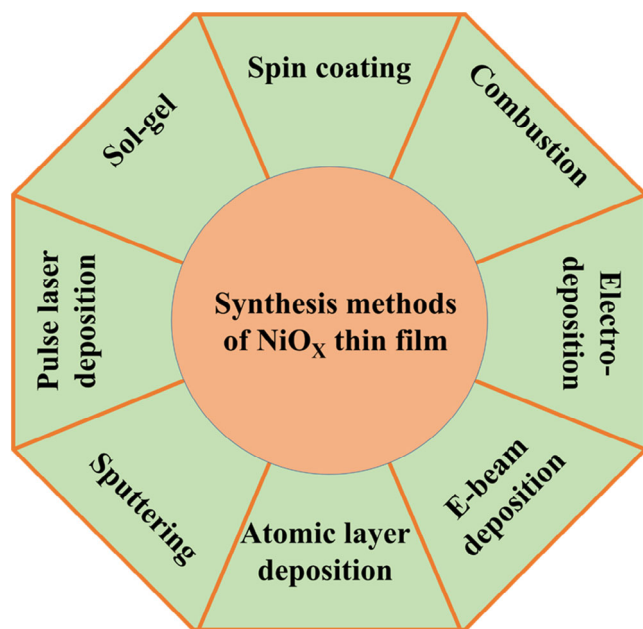


Figure 2. Synthesis methods of NiO_x thin films using the physical and chemical routes.

The synthesized NiO_x NP powder can be easily dissolved in solvents such as deionized water, isopropyl alcohol, etc, and the spin-casting process is frequently utilized to obtain a high-quality NiO_x film, in the range of nanometer-to-micrometer thickness, with the crystallized nanocrystals. In the spin-cast process, the substrate is kept on a chuck and rotates at the desired speed after the solution's dropping. The centrifugal force puts the solution outward, but the viscosity and surface tension help the growth of a uniform thin film. Finally, the thin film is heated at the desired temperature to remove organic contamination, and an additional high-temperature annealing can further enhance the crystallinity and grain size of NiO_x layer, affecting its morphology and the performances of PV cells built on the layer. The schematic representation of spin casting is shown in **Figure 3a**. Because the spin-cast NiO_x NPs can be annealed at low temperatures, various substrates can be utilized. However, this method significantly depends on the NiO_x NPs' quality, which requires the optimization of the synthesis platform. In addition, synthesizing NiO_x NP powder requires a lot of steps and time compared with other approaches. The surface morphology of NiO_x thin film is also significantly dependent on the quality of solution as well as the rotation speed, and thus dissolving NiO_x nanocrystals into the solvent is crucial. This affects the morphology of NiO_x film and finally the performance of the device.^[37,49,50] The high quality of HTL improves the morphology of the following perovskite layer and reduces the nonradiative recombination at the interface between HTL and photoactive layer.

Generally, NiO_x NPs can be prepared by thermally decomposing Ni(OH)₂ in a furnace. Ni(OH)₂ is synthesized by the reaction of nickel(II) nitrate hexahydrate (or nickel(II) chloride hexahydrate) with NaOH in DI water-based conditions (around pH 10).^[51,52] The NPs synthesized by this method have an average size ≈10 nm, and the prepared NiO_x thin film has rough morphology along with moderate density. The solar cell fabricated on the NiO_x film obtained by this method showed efficiency at around 17%,^[51–53] and it could be further enhanced up to 18.6% by the modifications of the absorber layer and the interface.^[54] This approach is convenient for the fabrication of flexible solar cells.^[51,55,56]

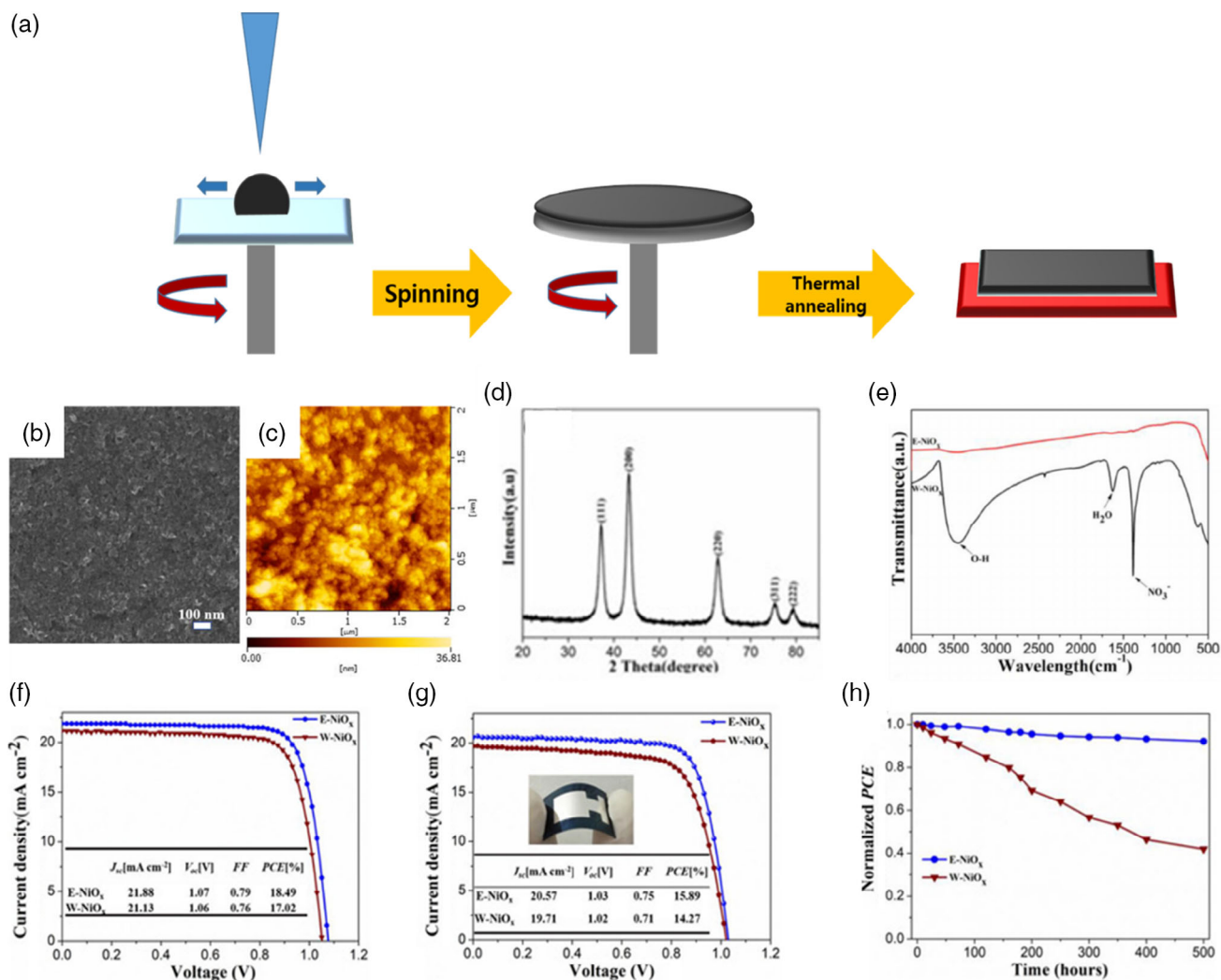


Figure 3. a) Schematic representation of spin-coating process. b) SEM, top view and c) AFM images of NiO_x NPs, which are dispersed in ethanol (E-NiO_x). d) XRD patterns of E-NiO_x. e) FTIR spectra of E-NiO_x and NiO_x NPs dispersed in water (W-NiO_x). f, g) *J*-*V* curves of rigid and flexible W/E-NiO_x-based perovskite PV cells. h) Normalized PCE of W/E-NiO_x-based perovskite PV cells. Reproduced with permission.^[57] Copyright 2018, WILEY-VCH.

Recently, high-quality NiO_x NPs were synthesized using stable ink in ethanol. The scanning electron microscopy (SEM) image ensured that the ethanol-dispersed NiO_x NPs covered the whole surface, as shown in Figure 3b. Moreover, the atomic force microscopy (AFM) image confirmed the smoothness of film, and its roughness was found at around 5.3 nm (Figure 3c). High-intense peaks of X-ray diffraction (XRD) patterns in Figure 3d validated the high crystallinity of the NiO_x film. Fourier-transform infrared spectroscopy (FTIR) characterization was also conducted to examine the formation of chemical bonds on the surface of NiO_x films (Figure 3e). No peaks were observed in the ethanol-dissolved NiO_x NPs, which confirmed the ligand-free behavior, whereas various peaks corresponding to water, hydroxyl groups, and other functional ligands on the surface were found from the water-dissolved NPs. *J*-*V* curves of rigid and flexible solar cells fabricated on NiO_x thin films showed 18.49% and 15.89% PCEs, respectively (Figure 3f, g).^[57]

The PSC, built on the ethanol-dissolved NiO_x NPs, retained 90% of initial efficiency after the 500 h, whereas the PSC device, prepared on water-dissolved NiO_x NPs, reduced to 40% of its initial efficiency, as shown in Figure 3h.

2.2. Sol-Gel Method

The sol-gel method is most frequently used to deposit the NiO_x films, due to its simplicity and good reliability. This method has advantages, such as low energy consumption and easy incorporation of atoms due to molecular-level mixing, but it has disadvantages like long processing time and difficulty in removal of hydroxyl and carbon groups. High-temperature annealing is another disadvantage preventing its industrial scale production. In this method, the metal precursors, usually utilized as stabilizing agents, are dissolved in the organic solvent. This solution is further used for the deposition of film using spin casting or spray

pyrolysis. As for the spin-cast films, those thin films should be annealed at a high temperature to remove the organic impurity and enhance their crystallinity and grain size. It is also observed that the bandgap is shifted toward lower energy with increasing the annealing temperature. The annealing atmosphere also affects the properties of NiO_x films. Zhao et al. synthesized NiO_x thin films using a sol-gel method and annealed them in air, O₂, N₂, and Ar atmosphere.^[58] It was shown that the electrical properties of NiO_x were modified with these atmospheres due to the formation of point defects. The resistivity values of NiO_x films were found in the order of Ar > N₂ > air > O₂, and higher mobility was observed from the film annealed in O₂ and air atmosphere, compared with those annealed in N₂ and Ar. High conductivity and mobility are advantageous for fast charge carrier transport, and improved PV performances were confirmed for the PSC devices with NiO_x annealed in the oxygen-rich atmosphere, compared with those with NiO_x prepared in inert condition.

Meanwhile, for spray pyrolysis, the substrate is often heated at the desire temperature, and crystallization can be affected by the deposition time. A schematic representation of thin-film deposition by the spray-pyrolysis method is shown in **Figure 4a**. Spray pyrolysis is a simple and inexpensive deposition method, and dense and large-scale NiO_x thin film can be obtained. There have been various approaches to prepare the solutions for sol-gel method-based NiO_x thin films, and a wide range of PCEs were

reported from the planar p-i-n PSCs.^[59–68] The one-step spin-casting process, followed by antisolvent treatment, has been widely used to grow high-quality perovskite films on NiO_x thin films, and PCEs close to 15% were reported.^[64,68] When the perovskite film was further heated in the presence of solvent vapor, the crystalline size increased; as a result, the PCE reached 17.64%.^[65]

Han and coworkers reported several works on the growth of NiO_x layer using the spray-pyrolysis method.^[69–71] The substrate temperature for the spray pyrolysis method was kept at around 500–560 °C, and a similar temperature was used during post-annealing to improve film crystallinity.^[72–74] The PSCs, based on the spray pyrolysis-cast NiO_x thin film and ethyl acetate-modified perovskite film, showed efficiency of around 15.58% and the *J*-*V* curve and SEM image of the device are shown in **Figure 4b,c**, respectively.^[70] They enhanced the efficiency of devices to around 17.6% over the 1 cm² active area, as shown in **Figure 4d**, and the SEM of the corresponding device is shown in **Figure 4e**.^[71] The maximum efficiency of PSCs, reported with the spray-pyrolyzed NiO_x, was 19.19% (**Figure 4f**), and the SEM image of the device is shown **Figure 4g**.^[69] The sol-gel method is one of the simplest methods to produce NiO_x thin film, but its necessity of high temperature annealing limits its application to the flexible solar cell fabrication. Moreover, additional additives such as stabilizing agent and surfactant for the chemical reaction on the substrate can be factors that reduce the purity of thin films when the annealing process is not conducted enough.

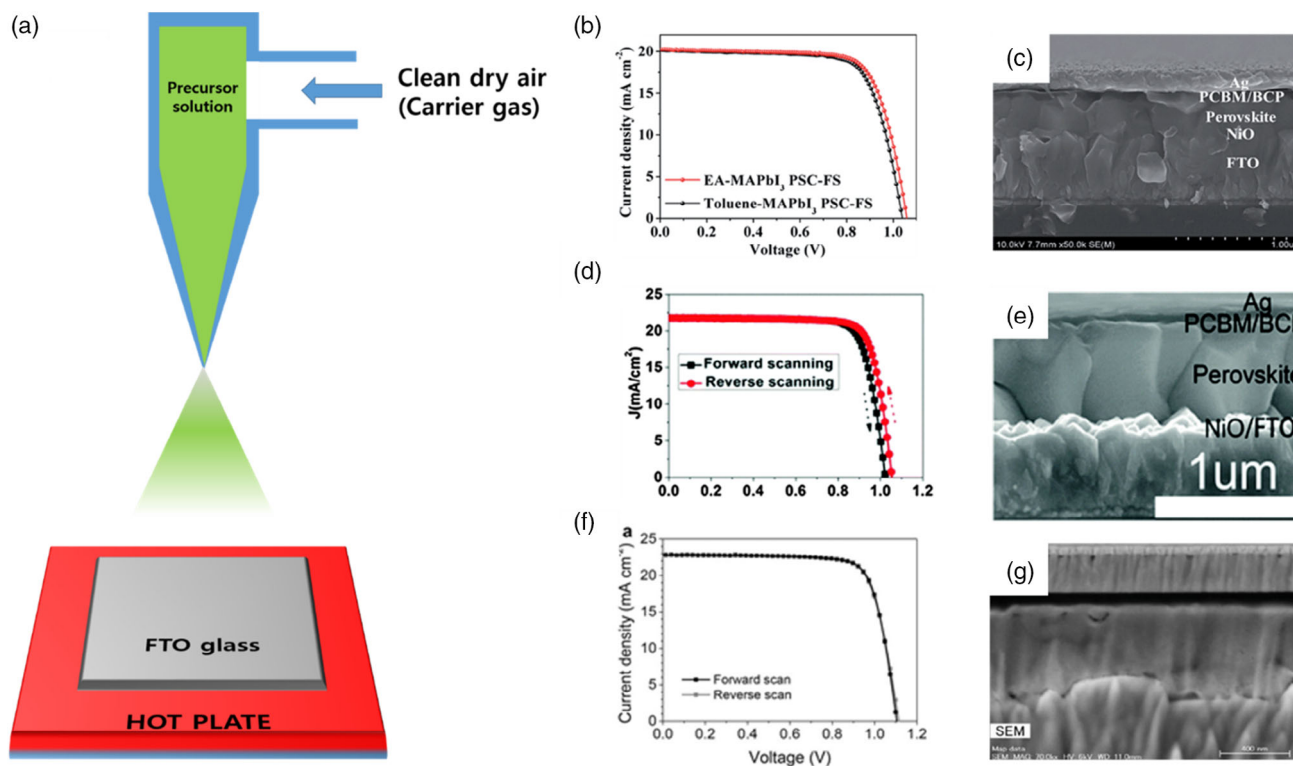


Figure 4. a) Schematic representation of spray-pyrolysis method. b,d,f) *J*-*V* curves of devices using NiO_x synthesized by spray pyrolysis. c,e,g) Cross-sectional SEM images of devices corresponding to each (b,d,f). Reproduced with permission.^[69–71] Copyright 2017, WILEY-VCH. Copyright 2016, The Royal Society of Chemistry.

2.3. Combustion Method

The combustion method is a self-propagating high-temperature synthesis method, because the heat, limited in a small quantity of precursors, easily dissipates due to the large surface-to-volume ratio of thin films. Therefore, the substrate is not significantly influenced by heat, and thus flexible plastic substrates can be used.^[75,76] Zhang and coworkers deposited the NiO_x thin film at 175 °C using the combustion method,^[77] and Jen and coworkers reduced the deposition temperature to 150 °C by replacing glycine with acetylacetone.^[78] Hao and coworkers synthesized NiO_x thin film and compared its properties with the sol-gel method-based thin film.^[79] Although the surface morphology and roughness were almost the same (Figure 5b–e), the XRD peaks of the combustion-based thin film were more intense than those of sol-gel-derived thin film, ensuring higher crystallinity of the combustion-based thin film even with its lower processing temperature (Figure 5a). Furthermore, the combustion-based NiO_x thin film was confirmed to have high transmittance

(Figure 5f), and steady-state and time-resolved photoluminescence (PL) results represented efficient charge extraction at the interface between perovskite and combustion-based NiO_x thin film (Figure 5g,h). The PSC device, built on the combustion-based NiO_x thin film, showed maximum PCE of 20.2% with high stability and low hysteresis (Figure 5i–k).

Combustion methods can save time and energy compared with other deposition methods. The strength and feature of this method are that it can induce an exothermic reaction based on chemical reaction mechanism without additional heating from outside. However, the major drawback of this method is that the chemical reaction may produce unreacted precursors. Moreover, if the reaction is not controlled uniformly throughout the reaction area, the size distribution of oxide particles will increase, reducing the uniformity of the film. These chemical and structural issues can act as defects in PSCs, and therefore, this method should be optimized by comparing and analyzing the properties of thin films and processing conditions.

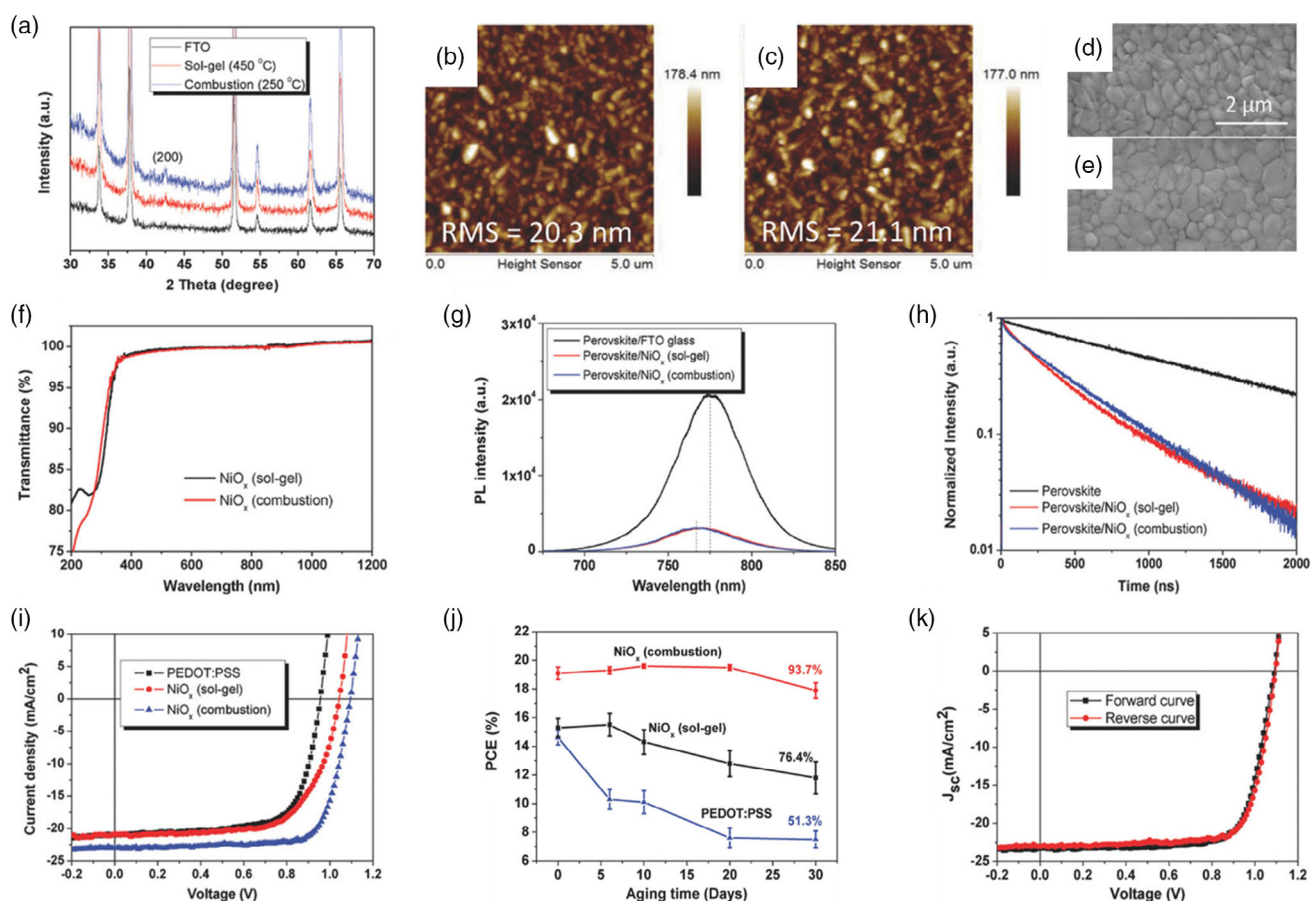
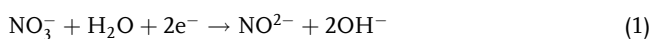


Figure 5. a) XRD patterns of FTO substrate, sol-gel, and combustion method-processed NiO_x films. AFM images of b) sol-gel- and c) combustion-processed NiO_x thin films. Top-view SEM images of the perovskite films deposited on d) sol-gel- and e) combustion-processed NiO_x thin films. f) Absorption coefficient as a function of photon energy for sol-gel- and combustion-processed NiO_x thin films. g) Steady-state PL spectra of perovskite films deposited on the sol-gel- and combustion-processed NiO_x thin films. h) Time-resolved PL of perovskite films deposited on the sol-gel and combustion-processed NiO_x thin films. i) *J*–*V* curves of perovskite PV cells based on different HTLs. j) Ambient air stability of unencapsulated perovskite PV cells based on different HTLs. k) *J*–*V* curves of perovskite PV cells based on combustion-based NiO_x. Reproduced with permission.^[79] Copyright 2018, WILEY-VCH.

2.4. Electrodeposition

Electrodeposition is a simple and cost-effective method to deposit NiO_x films, which have potential for large-scale mass production. Moreover, it has numerous advantages such as low-energy consumption, less safety, and minimum production of byproducts for disposal. The electrodeposition process of NiO_x thin film is usually composed of two steps: the first step is the deposition of Ni(OH)₂ from nickel precursor, and the second step is annealing Ni(OH)₂ thin film at the desire temperature to obtain NiO_x thin film.^[32,80,81] Nickel nitrate is frequently used as an electrolyte, and nitrate ion is converted to nitrile ion in the presence of H₂O, providing hydroxyl ions. The nickel and hydroxyl ions produce nickel hydroxide, and it is deposited on the substrate. Further heating above 300 °C converts it to NiO_x. The electrochemical deposition process of NiO_x thin film can be explained with the following equation



The surface uniformity of NiO_x thin films, prepared at different current densities of 0.1, 0.2, and 0.5 mA cm⁻², was investigated by AFM and SEM (Figure 6a), and it was further examined by the cross-sectional SEM images (Figure 6b).^[81] Those results showed that the surface roughness of the NiO_x film decreased from 5.0 to 2.1 nm with the change in current density from 0.1 to 0.5 mA cm⁻² (Figure 6c). Figure 6d shows the effect of current density on the surface morphology of Ni(OH)₂ along with total number of charges. It was shown that the porous, rougher, and thicker NiO_x film, deposited at 0.1 mA cm⁻², was beneficial for obtaining PSCs having a high fill factor (FF) without degrading *J*_{sc} and *V*_{oc}, as shown in Figure 6e.^[81] The fabricated device showed a maximum PCE of 17.0% with an active area of 1.084 cm² (Figure 6f), and its external quantum efficiency (EQE) signals are shown in Figure 6g.

Electrodeposition is a method that allows uniform and nanostructured thin films to be deposited on a large area by the electrochemical process. Therefore, it is one of the promising methods for the commercialization of PSCs. It can easily adjust the thickness of NiO_x thin film by controlling deposition time and applied current. However, its usage on the flexible substrate is restricted due to its high-temperature annealing process. In addition, when the deposition current is low, voids are generated in the film, and they increase the roughness of the film. Those rough films can transpire the undesirable performance of PSCs. Accordingly, optimization of the processing condition is necessary.

2.5. Pulsed Laser Deposition

Despite the advantages of solution-processed NiO_x such as low cost and simple processability, they are known to have various defects, degrading light transmittance and carrier transportation characteristics. Pulsed laser deposition (PLD) method has been widely utilized for the deposition of high-quality thin films.

This process uses a high-power pulsed laser beam that strikes the target in an ultrahigh vacuum chamber. The targeted material is evaporated to form the plasma plume and then deposited on the substrate. This is a simple reactive deposition process that can maintain the exact stoichiometry of the film with relatively high deposition rates. Due to the ejection of high-energy particles from the target with the help of laser plume, the PLD film has high crystallinity even at a relatively low temperature. The schematic representation of PLD method is shown in Figure 7a. Park et al. synthesized the “nanostructured” NiO_x films using this PLD method, and those well-organized NiO_x nanostructured thin films, positioned at the bottom of the perovskite, improved PV device performances.^[82] As shown in the cross-sectional and top-view SEM images of NiO_x films, deposited at different oxygen partial pressures (Figure 7c), their morphology and corresponding properties could be controlled by adjusting the partial oxygen pressure and laser power. The schematic representation of thin-film growth at different oxygen pressures is shown in Figure 7d. Their porosity and roughness increased with the partial oxygen pressure during the process, and thus their transmittance in the visible wavelength range, under the same thickness condition, increased with the oxygen pressure (Figure 7g). However, the “disordered” NiO_x thin film having high porosity, prepared at the highest oxygen pressure condition, was not efficient for hole extraction. XRD patterns also showed that its crystallinity and orientation decreased with the oxygen pressure (Figure 7f). At 200 mTorr oxygen pressure, NiO_x nanostructure had high crystallinity, oriented along (111) plane, whereas its crystallinity and orientation degraded at higher pressure conditions.

J-*V* curves of PSCs with NiO_x layers, prepared under different oxygen pressure conditions, are shown in Figure 7e, and a maximum PCE of 17.3% was achieved from the “nanostructured” NiO_x films, processed at 200 mTorr oxygen pressure condition (Figure 7b). The enhanced performance in a nanostructured NiO_x film was attributed to the slow recombination rate during the extraction and transport of the dissociated carriers. As a result, the (111)-oriented nanostructured NiO_x film with good optical transparency played a key role in the efficient extraction of holes and the prevention of electron leakage as an HTM in a PSC. However, the PLD method has some limitations on large-scale growth and conformal coverage, and those have limited the application of the PLD method to the large-scale production of PSCs.

The NiO_x thin films, deposited by low-temperature solution processes, have structural defects, and these defects reduce charge carrier extraction and transportation capability of NiO_x thin film. In this aspect, the PLD method that can improve the film uniformity and density is highly desirable. Furthermore, it can precisely control the thickness of the film by controlling the deposition parameters (i.e., O₂ partial pressure and deposition time), and it can be processed at low temperatures without direct heat energy, applied to the substrate, promising flexible PSC fabrication. Nevertheless, high energy, required for the direct plasma treatment on a target material, can be a difficulty in depositing the NiO_x thin film using this approach. In addition, an expensive equipment to maintain an ultrahigh vacuum condition during the deposition process is needed, and the area and the number of substrates are limited to the chamber size.

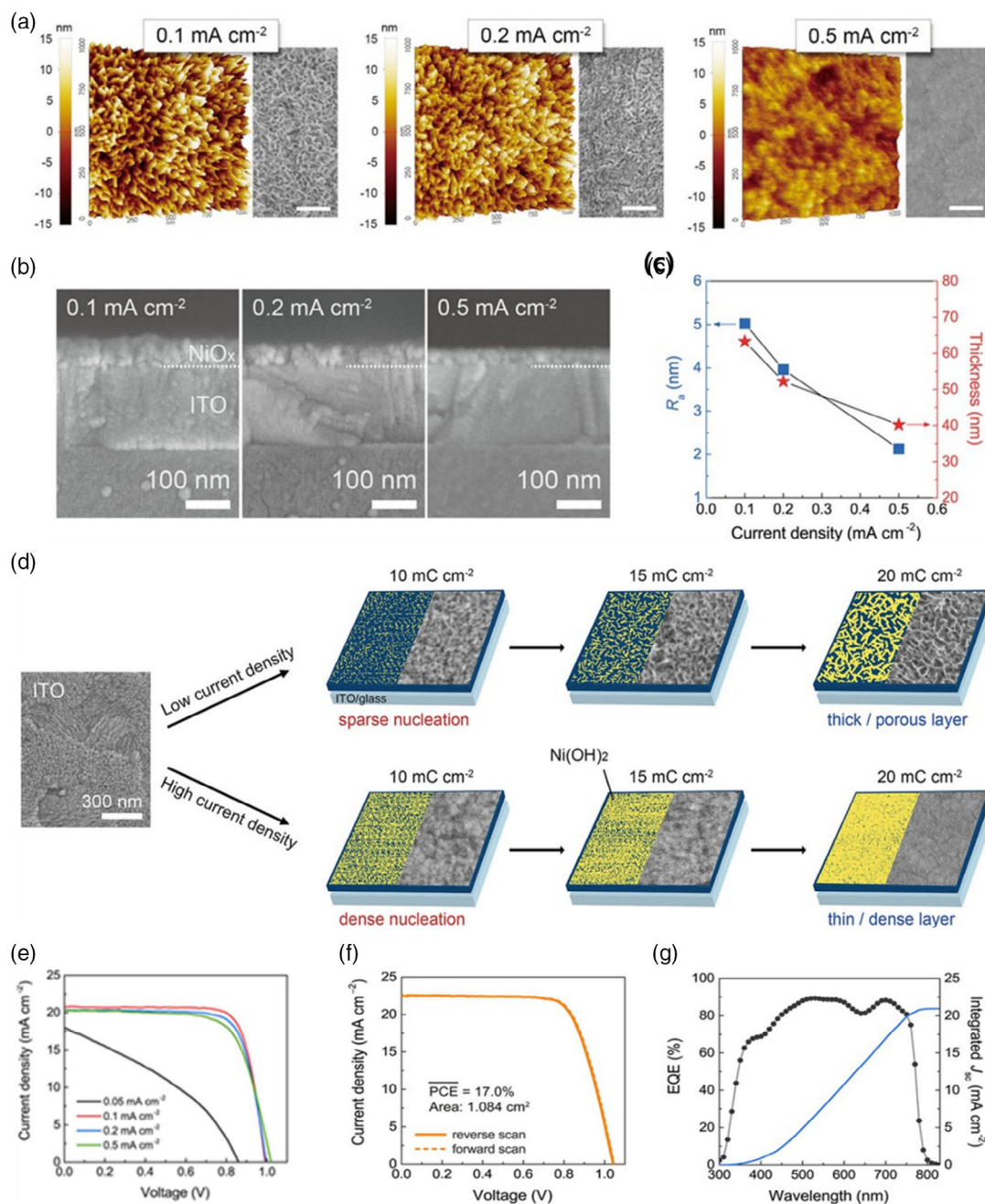


Figure 6. a) 3D AFM and top-view SEM images of the NiO_x surface with different current densities (scale bar: 200 nm). b) Cross-sectional SEM images of the ITO/NiO_x layer with different current densities. c) Average roughness factor and thickness of the NiO_x layer with different current densities (blue square: average roughness, red star: thickness). d) Schematic showing corresponding SEM images of the Ni(OH)₂ electrodeposition method with different total charges. e) *J*-*V* curves of perovskite PV cells with an electrodeposited NiO_x layer deposited at various current densities. f) *J*-*V* curves of the best-performing device (active area of 1.084 cm²). g) EQE spectra and integrated *J*_{sc}. Reproduced with permission.^[81] Copyright 2017, WILEY-VCH.

2.6. E-Beam Deposition

A schematic representation of e-beam deposition is shown in **Figure 8a**. When a source material is targeted by a high-energy electron beam, the electron loses their energy, instantly inducing large thermal energy, useful for evaporation. For the NiO_x

thin-film formation, Ni metal is utilized as a source material, and its stoichiometry varies with the annealing temperature and flow rate of oxygen.^[36,83] The Ni ion reacts with the oxygen atom, consequently forming NiO_x at a certain annealing temperature. **Figure 8b,c** shows SEM images of NiO_x films, prepared by vacuum-assisted e-beam deposition and solution-based spin

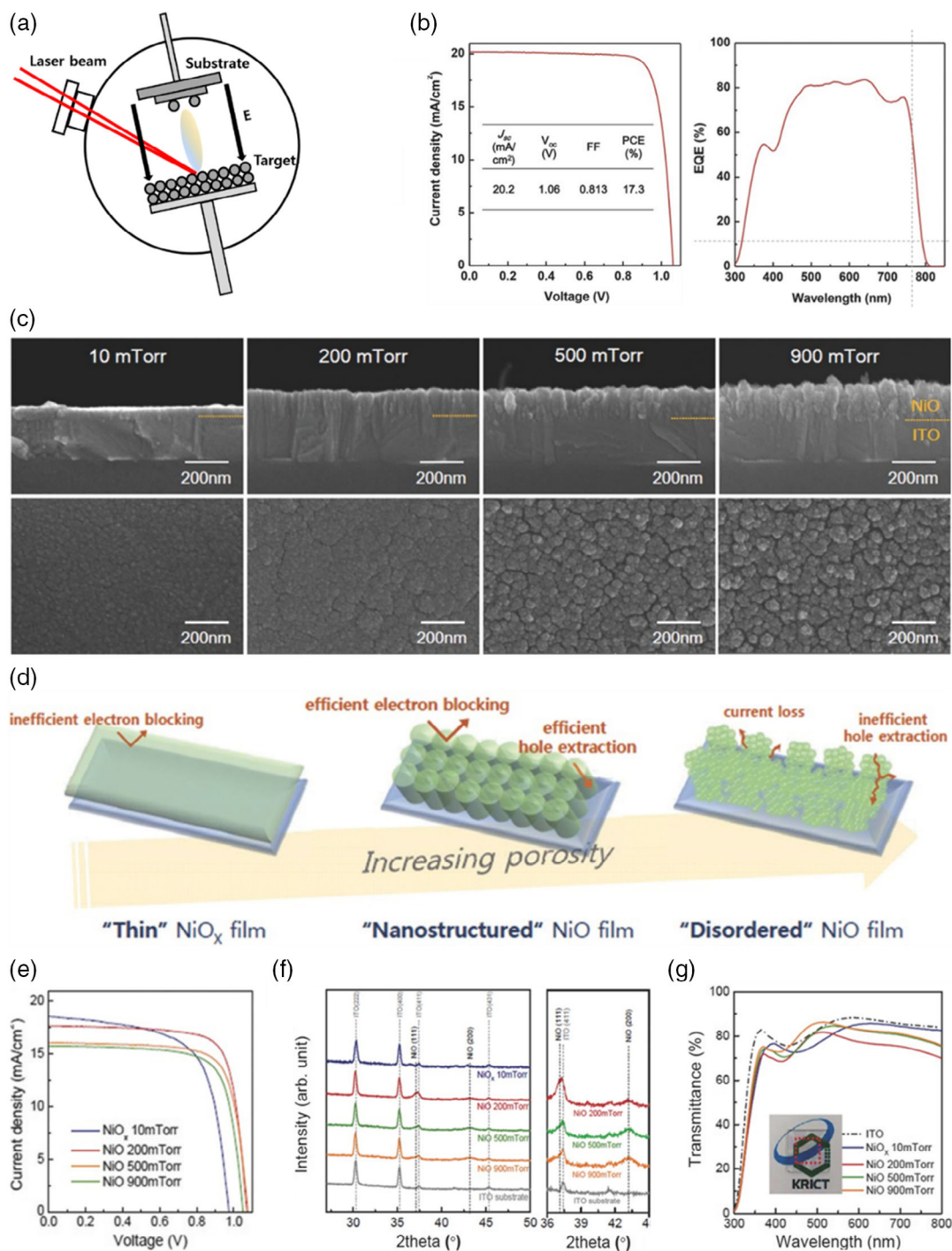


Figure 7. a) Schematic representation of PLD. b) J – V curves (left) and EQE (EQE, right) for the best cell using nanostructured NiO_x film with thickness of 150 nm. c) Cross-sectional and top-view SEM images of the NiO_x films synthesized by PLD. d) Schematic images of thin, nanostructured, and disordered NiO_x films synthesized by PLD as an electron blocking layer/hole extraction layer in the perovskite-PCBM heterojunction PV cells. e) J – V curves of PSCs based on PLD- NiO_x films, deposited at various oxygen partial pressures. f) High-resolution XRD (HR-XRD) patterns of the NiO_x films synthesized by PLD. g) Transmittance spectra of the NiO_x films synthesized by PLD. Reproduced with permission.^[82] Copyright 2015, WILEY-VCH.

casting, respectively. The e-beam-deposited NiO_x thin film had larger grain size than the spin-cast film (Figure 8b,c), and the PSCs with the e-beam-deposited NiO_x showed higher efficiency

and reproducibility (Figure 8d). Moreover, lower PL intensity of the perovskite film cast on the e-beam-deposited NiO_x confirmed its efficient charge extraction from the photoabsorber (Figure 8e).

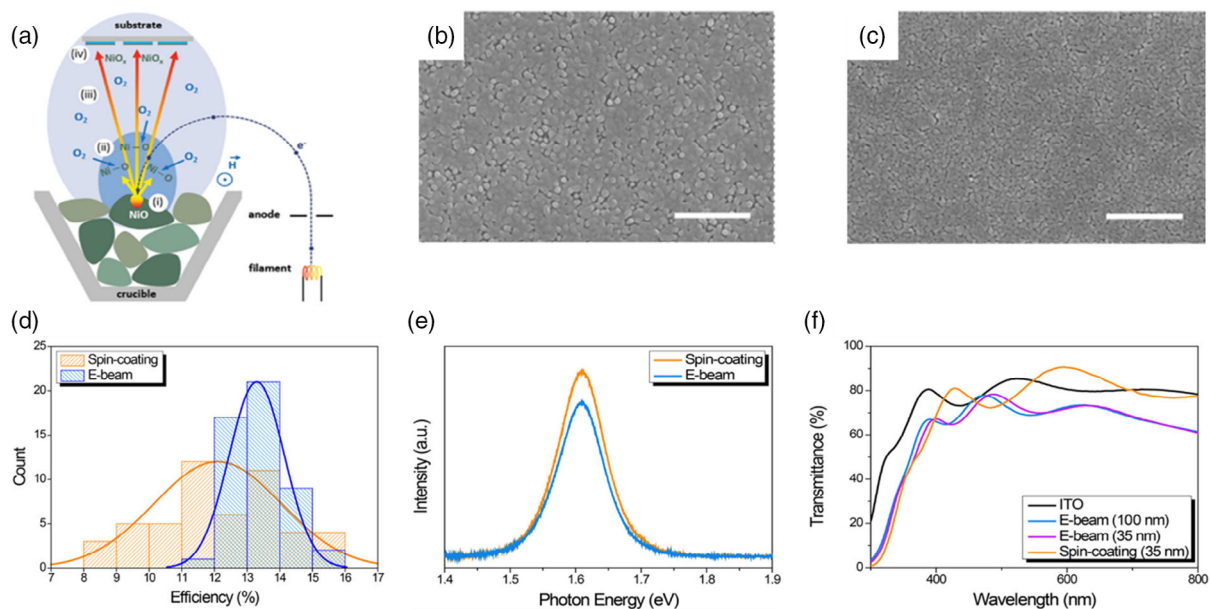


Figure 8. a) Schematic representation of e-beam deposition process. Reproduced with permission.^[36] Copyright 2019, WILEY-VCH. Top-view SEM images of b) e-beam-deposited and c) spin-coated NiO_x thin film on ITO glass. d) Histogram of perovskite PV cells with spin-coated and e-beam-deposited NiO_x thin film. e) PL spectra of $\text{CH}_3\text{NH}_3\text{PbI}_3$ on spin-coated and e-beam-evaporated NiO_x thin film and f) optical transmission spectra for ITO and NiO_x deposited on ITO via spin coating and e-beam evaporation. Reproduced with permission.^[83] Copyright 2018, American Chemical Society.

It was also shown that more Ni^{3+} in e-beam-evaporated NiO_x resulted in lower transmittance but it provided higher conductivity (Figure 8f). In addition, the solution-processed method has an uneven layer formation due to the accumulation of solution at the edge of the substrate, and thermal annealing treatment, generally required for the solution-processed NiO_x , is not desirable for large-scale production and is known to induce lots of defects in the thin film. Most of these disadvantages are expected to be resolved by the e-beam-evaporated NiO_x that can provide improved uniformity and compactness.

E-beam evaporation is one of the widely utilized methods for deposition of oxide-based thin films. The thickness and characteristics of the thin film can be easily adjusted through partial pressure or flow control of oxygen gas. However, there is still difficulty in commercialization because it requires high power and high-purity gas. To address these challenges, research has been conducted to form high-quality NiO_x thin films using e-beam deposition without the oxygen supply from outside.^[84,85] This simplification is expected to make it a little closer to commercialization.

2.7. Sputtering Process

In this process, ionized gas particles having high energy are bombarded to the source target, from which atoms are ejected and condensed at the substrate. For the synthesis of NiO_x thin film, Ni target with O_2 gas or NiO_x target can be utilized. As for the process with Ni target, Ni atoms are released from the target and react with oxygen atoms, consequently being deposited on the substrate in NiO_x thin-film format. During this process, various

factors such as the amount of oxygen, temperature of the substrate, and power affect the properties of NiO_x thin film.^[47,81,86,87] The growth orientation of sputtered NiO_x films mainly depends on the sputtering power and the substrate temperature. Use of a new reactive magnetron sputtering technique was discussed for gaining good coverage and junctions between the perovskite and NiO_x layer at low deposition temperature. The limitations of low FF and short-circuit current, commonly observed in sputtered NiO_x -derived PSCs, can be overcome through magnesium doping and low-oxygen partial pressure deposition. Li et al. demonstrated large-scale Mg-doped NiO_x (over an area of 100 cm^2) using the sputtering process for PSC devices.^[88] SEM images in Figure 9a,b show that morphology of perovskite is not significantly changed with Mg doping, but energy band of NiO_x can be improved for better alignment with the valence band edge of the perovskite layer (Figure 9c), inducing better charge extraction (Figure 9d). Consequently, the performances of PSC devices with the sputtered NiO_x thin film, which were usually inferior to those with the solution-processed NiO_x due to its low electrical conductivity and transmittance,^[89–92] were enhanced with Mg doping, leading to 18.5% PCE by improving its optoelectronic properties.^[88] The large-scale device also showed good uniformity and excellent stability in ambient condition (50–70% humidity), preserving 90% of its initial PCE after 600 h.

Sputtering process is suitable to fabricate high-quality thin films at low temperatures. Typically, radio frequency (RF)-type sputtering is used to deposit semiconductors such as NiO_x that can be processed approximately ten times faster than DC sputtering methods. This method is also appropriate for doping various types of metals, which can control the electrical properties of

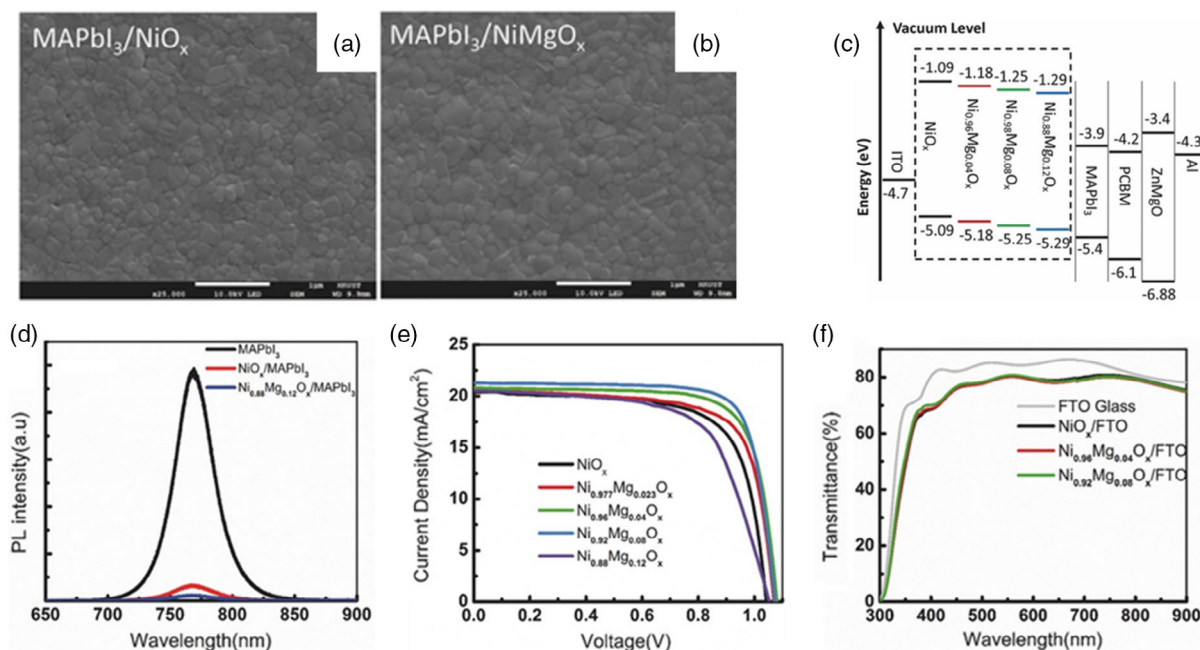


Figure 9. Top-view SEM images of CH₃NH₃PbI₃ films deposited on a) NiO_x and b) Ni_{0.92}Mg_{0.08}O_x. c) Energy-level diagrams of the investigated NiO_x and NiMgO_x in a perovskite PV cell structure. d) PL spectrum of CH₃NH₃PbI₃ deposited on glass (black line), NiO_x, and Ni_{0.92}Mg_{0.08}O_x, respectively. e) J–V curves of NiO_x- and NiMgO_x-based PSCs and f) transmittance spectra of NiO_x and NiMgO_x.^[188] Copyright 2017, WILEY-VCH.

thin films. However, it is difficult to apply this approach to large-area PV devices because uneven layers are easily formed on the large-area substrates.

2.8. Atomic Layer Deposition (ALD)

A schematic representation of the atomic layer deposition (ALD) process is shown in **Figure 10a**. For NiO_x thin-film formation by the ALD process, nickel-bis(1-dimethylamino-2-methyl-2-butanolate) and O₃ were utilized as precursors of Ni and O. The surface uniformity of NiO_x film was confirmed by AFM (root mean square in the range from 0.3 to 0.4 nm) (**Figure 10c**), and the top-view SEM image of perovskite layer in **Figure 10b** ensured dense growth of crystallized grains with an average size of 100–150 nm.^[93] The electrical conductivity and work function of the synthesized NiO_x thin film decreased, as its thickness was increased to 7.5 nm, and they saturated over this thickness. (**Figure 10d**). Space-charge profiles depending on the physical film thickness of NiO_x relative to Debye's length (*L_D*) are shown in **Figure 10e**. If the thickness of NiO_x is large enough compared with *L_D*, it behaves like an insulator, but if it is thin enough, *L_D* starts to overlap, enhancing its work function and electrical conductivity. This is correlated with the results in **Figure 10d**, where the work function and electrical conductivity increase with the reduction in its thickness. Correspondingly, the maximum PCE at around 11.82% was obtained from the 5 nm NiO_x, because this thickness was sufficient for *L_D* to be overlapped. The efficiency of PSCs could be further improved by post-heat treatment of NiO_x film. Mott–Schottky plots in **Figure 10g** confirmed that work function and electrical conductivity of NiO_x film

increased with postannealing. X-ray photoelectron spectroscopy (XPS) analyses of pristine and annealed NiO_x (**Figure 10h**) show that Ni oxidation states are changed and the amount of water and hydroxyl group is reduced after annealing, which improves the interfacial properties. Due to improvement in the work function and electrical conductivity, the PCE of annealed NiO_x-based PSCs was further enhanced to 16.4% (**Figure 10i**).

The ALD method has a great merit that can provide highly uniform thin films through direct chemical reactions on the surface of the substrate. However, this method demands not only high-purity precursors, but also multiple pulse–purge cycles, resulting in high cost and long processing time, compared with other methods. Therefore, to further improve the usability of this method, modification of the chemical reaction mechanism and reduction of the process time should be considered.

3. Modification of NiO_x Properties and NiO_x/Perovskite Interface

Significant progress in NiO_x-based planar p–i–n PSCs is made, but their PCEs are still less than those of poly(triaryl amine) (PTAA)-based PSCs, showing the best efficiency of 23.0% in p–i–n structures,^[94] due to their low electrical conductivity, low transmittance, rough surface morphology, and unoptimized energy level. Doping NiO_x thin films with extrinsic elements and modifying their surface with the organic and inorganic materials are widely investigated approaches to overcome those limitations as a HTM of PSC devices (**Figure 11**). Especially, dopants significantly influence their optoelectronic properties by adjusting their stoichiometry, oxidation states, and band structure; thus,

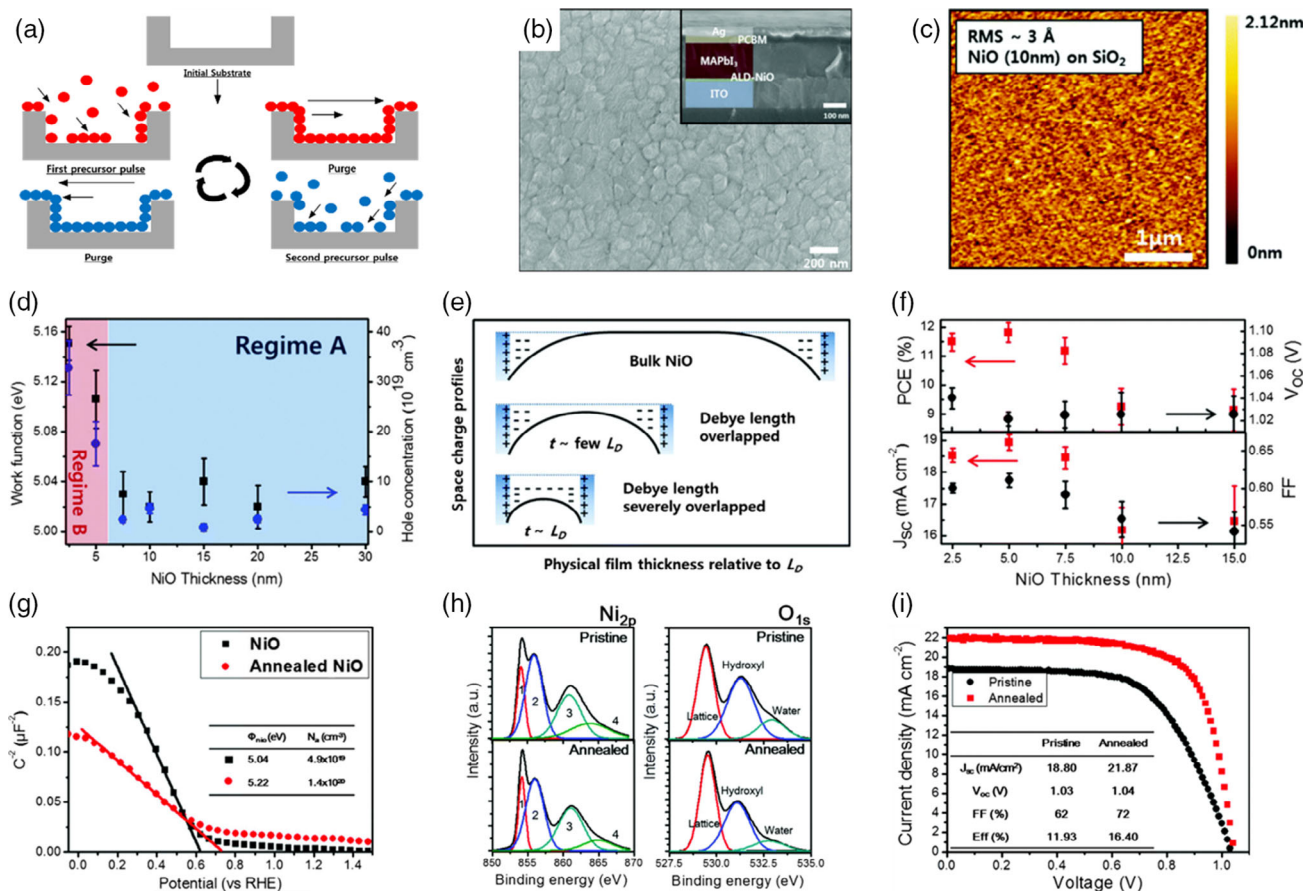


Figure 10. a) Schematic showing the process of ALD. b) Field-emission SEM (FESEM) image of the morphology of perovskite thin film on ALD-NiO_x and inset shows the cross-sectional SEM image of the completed device. c) AFM image of ALD-NiO_x thin film on a SiO₂/Si substrate. d) Plot of the work function (E_{fb}) and hole concentration (N_{a}) versus the thickness of ALD-NiO_x thin film measured by electrochemical Mott–Schottky analysis. Black squares and blue circles indicate the work function and doping concentration, respectively. e) Schematic showing the physical film thickness relative to the Debye length (L_{D}) versus space–charge profiles. f) Top plot shows the PCE and open-circuit voltage (V_{oc}) versus the thickness of ALD-NiO_x thin films. g) C^{-2} – V plot for pristine (black squares) and annealed (red spheres) ALD-NiO_x thin films measured by Mott–Schottky impedance analysis. h) XPS data of the pristine (top) and annealed (bottom) ALD-NiO_x thin films. i) J – V curves for best cells of pristine (black circles) and annealed (red squares) ALD-NiO_x thin films with a thickness of 7.5 nm. Reproduced with permission.^[93] Copyright 2016, The Royal Society of Chemistry.

enhancement in conductivity, transmittance, and work function is observed. It is interesting to note that the stoichiometric NiO_x shows insulating behavior, but it exhibits p-type conductivity after the alteration of its stoichiometry by self-creating Ni vacancy.^[95] Dopants also play a vital role in improving their crystallinity and alleviating surface traps, which contribute to improving the stability and reproducibility of PSC devices with negligible hysteresis loss. So far, various elements, such as transition metals, alkali metals, alkaline earth metals, nonmetal elements, and rare-earth metals, have been used as suitable dopants for NiO_x. Moreover, the surface functionalization of NiO_x films also has shown significant progress to improve the PCEs of PSCs.

3.1. Transition Metals Doping

The research works of transition metal doping in NiO_x are almost exclusively dominated by the p-type dopants like Co and Cu.^[96,97] Nevertheless, some other elements such as Fe, Zn, Ag, and

Al have also been attempted.^[98–101] Chen et al. improved the carrier mobility of NiO_x by adding Cu, consequently increasing its conductivity significantly, verified by the conductive AFM (c-AFM) and I – V analysis (Figure 12a–c).^[102] Theoretically calculated density of states (DOS) showed that Cu-doped NiO_x had the gap state at ≈ 0.7 eV above the Fermi level, whereas Ni vacancies in bulk NiO had the gap states at ≈ 1.3 – 2.0 eV above the Fermi level, which represented that Cu doping produced shallower acceptor levels, increasing hole concentration, conductivity, and work function. Furthermore, Cu⁺ could be substituted for Ni²⁺, contributing to the improvement of carrier concentration and carrier mobility, and lower monomolecular Shockley–Read–Hall recombination decreased the recombination loss. Consequently, after adding Cu dopant, the inferior hole-extraction ability at the interface between NiO_x and perovskite was improved, enhancing the performances of PSC devices.

Bashir et al. also have intensively investigated Cu doping of NiO_x, and they observed an increment in electrical conductivity

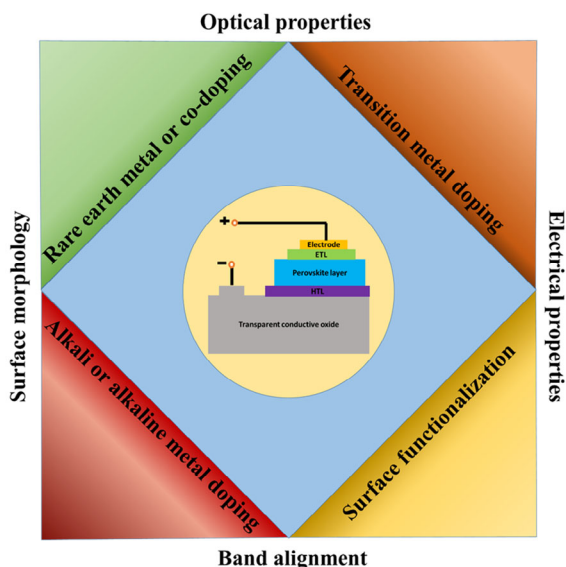


Figure 11. Schematic representation of different types of modifications used to modify the NiO_x thin film and their impact on various properties.

from 2×10^{-3} to 0.20 S cm^{-1} after the addition of 5% Cu dopant due to the reduction of bandgap from 3.25 eV (pristine NiO_x) to 3.12 eV, as shown in Figure 12d.^[103] Moreover, Cu-doped NiO_x had a higher crystallite size (19.6 nm) than pristine NiO_x (12.89 nm), which indicated that the Cu content can promote the sustained growth of more widely dispersed nuclei of NiO_x film. Thus, losses in J_{sc} and FF in the pristine NiO_x-based PSCs were mitigated, and the PCE increased from 10.49 to 12.79%. Subsequently, Feng et al. studied the influence of Cu doping concentration on NiO_x for PSCs.^[97] The Cu doping

did not change the surface morphology significantly, but it reduced the surface roughness (Figure 12e,f), which could be beneficial for the pinhole-free and smooth surface formation. Cu-doped NiO_x HTL-based PSCs achieved the highest PCE of 20.41% with J_{sc} of 23.17 mA cm^{-2} , as shown in Figure 12g.

Various research works have been conducted to further improve the functional properties of the Cu-doped NiO_x HTL, such as UV–O₃ treatment,^[104] organic surface modification,^[105] addition of mesoporous layer, etc.^[106] For instance, He et al. passivated Cu-doped NiO_x HTLs using different small molecules such as glycine, cysteine, and mercaptoethylamine chlorate. Among these, the PSC with cysteine-modified Cu:NiO_x HTL exhibited the PCE over 18% mainly due to the improvement of J_{sc} and V_{oc} .^[107]

In contrast, as a neighbor of Ni, Co was used as a suitable p-type dopant for NiO_x due to the similar atomic radii of Co (152 pm) to that of Ni (149 pm). Huang et al. first introduced sputtered Co-doped NiO_x HTL for planar PSCs. With the dramatic improvement in J_{sc} and FF, they obtained 25% higher efficiency than that of undoped NiO_x (from 9.46% to 12.61%).^[108] The enhancement of hole mobility (from 3.718×10^2 to $3.232 \times 10^3 \text{ cm}^2 \text{ V}^{-1} \text{ S}^{-1}$) and improvement in surface roughness (from 12.691 to 5.545 nm) reduced the electrical and optical loss. As a result, the device showed only 90% PCE retention even after 10 days of storage without encapsulation. After that, Xie et al. fabricated planar PSCs using simple solution-processed Co-doped NiO_x as HTL.^[109] They investigated the effect of Co doping concentration on the optoelectronic properties of NiO_x. Based on optimization, 6 mol% of Co-doped NiO_x exhibited a superior PCE of 18.2%, compared with 17.2% of undoped counterparts. All the device characteristics such as J_{sc} , V_{oc} , and FF increased by Co doping due to the enhanced electrical conductivity and reduced interfacial accumulation of charge

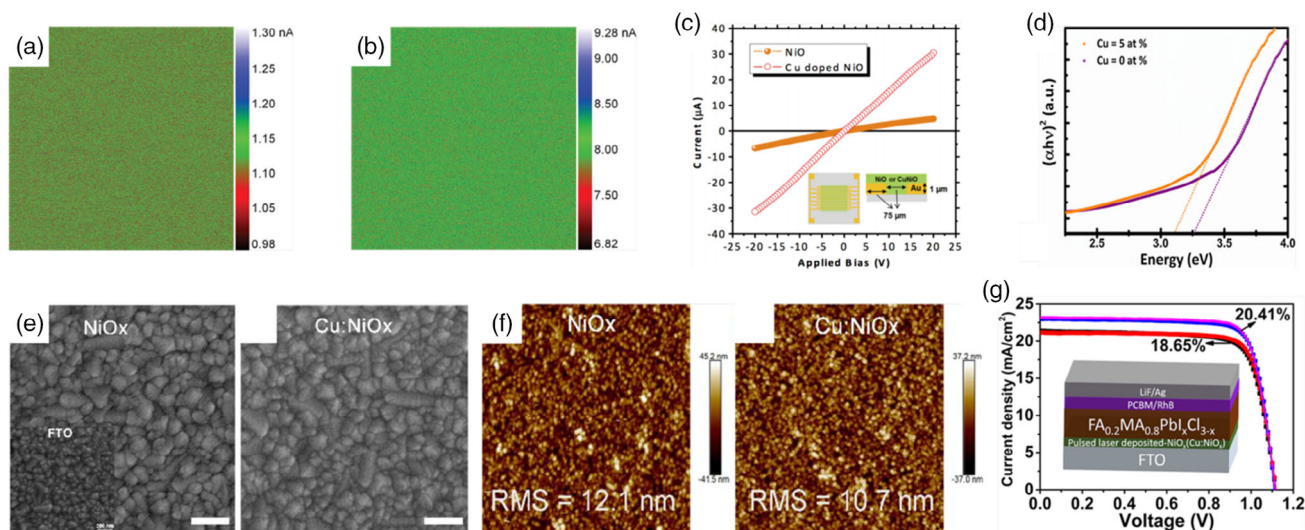


Figure 12. a) c-AFM images of a) NiO_x and b) Cu-doped NiO_x thin films on ITO glass. c) I – V curves of NiO_x and Cu-doped NiO_x measured using Au interdigitated electrodes with an electrode distance of 75 μm. Reproduced with permission.^[102] Copyright 2018, WILEY-VCH. d) Comparison of energy bandgap pristine NiO_x (3.25 eV) and Cu-doped NiO_x (3.12 eV). Reproduced with permission.^[103] Copyright 2019, Elsevier. e) Top-view SEM images of NiO_x and Cu-doped NiO_x thin film on FTO glass. f) AFM images of NiO_x and Cu-doped NiO_x thin film on FTO glass. g) J – V curves of best performing PSC devices with Cu-doped NiO_x, deposited by PLD, and with undoped NiO_x. Reproduced with permission.^[97] Copyright 2020, American Chemical Society.

carriers. Subsequently, Jung and coworkers improved the PCE of PSCs from 13.96% to 17.52% through 5% Co doping.^[110] This improvement was mainly attributed to the enhanced electrical conductivity, better energy band alignment, and reduction of surface trap sites. The improved interface of Co–NiO_x/perovskite increased the grain size of perovskite to as high as 500 nm, which strongly reduced the trap sites at the grain boundary.

Silver (Ag) has been also used as a p-type dopant, and many research works have been conducted to improve the optoelectronic properties of metal oxide thin films using Ag as a dopant.^[111–113] Wei et al. applied Ag dopant in NiO_x HTL by solution-based spin casting for p–i–n PSCs.^[98] Their density functional theory (DFT) calculations showed that Ag occupied the substitutional Ni site (Ag_{Ni}), and 2 at% Ag was experimentally confirmed as an optimum condition. Compared with pristine NiO_x, the Ag-doped NiO_x increased the efficiency from 13.46% (pristine NiO_x) to 16.86% (2 at% Ag-doped NiO_x). This enhancement was strongly attributed to the appropriate Ag doping, which improved the functional properties of NiO_x films such as optical transparency, work function, electrical conductivity, and hole mobility. Furthermore, the efficient charge carrier extraction from the perovskite was also confirmed by PL lifetime decrease of the perovskite cast on Ag-doped NiO_x HTL (from 17.0 to 5.5 ns). In addition, the PSCs with Ag-doped NiO_x stably operated without hysteresis and their stability was also improved.

Recently, aluminum (Al) doping strategy, which can increase the efficiency over 20%, was suggested.^[99] The enhanced electrical conductivity of Al-doped NiO_x significantly reduced the nonradiative recombination losses at the interface between HTL and perovskite. From the Kelvin probe analysis, the surface potential of Al-doped NiO_x was confirmed to be 603 mV lower than that of the pristine one. The PSC device with Al-doped NiO_x HTL showed the PCE of 20.84% (J_{sc} of 24.34 mA cm⁻², V_{oc} of 1.06 eV, and FF of 81.31%) with negligible hysteresis, which exceeded to the device with pristine NiO_x HTL (PCE 16.56%). Moreover, the devices with Al-doped NiO_x HTL retained 84.3% of their initial efficiency after 72 days and stabilized output PCE of 19.91% at maximum power point tracking.

In contrast, n-type element zinc (Zn) was also utilized as a dopant for NiO_x.^[100] It is well known that zinc is an Earth-abundant low-cost element and it is more applicable for the solution-processed techniques. The 5% of Zn-doped NiO_x exhibited high current flow with a scale of 5 nA in c-AFM measurement compared with that of NiO_x, which was attributed to the Zn dopant-induced charge carrier concentration. It also afforded high-quality perovskite with a large grain size of 500 nm, which reduced the trap site density at the grain boundaries. As a result, a noticeable improvement in PCE was observed from 10.43% to 13.72%.^[87]

Chandrasekhar et al. tried iron (Fe) as a dopant for NiO_x HTL using NP ink at room temperature.^[101] Fe doping resulted in a favorable work function and enhanced conductivity, which improved the hole extraction and reduced the recombination losses at the interface. The PCE of PSCs increased from 15.41% to 17.57% for rigid and from 13.37% to 14.42% for flexible devices with the Fe-doped NiO_x HTL. **Table 1** and **2** show the performance of PSCs based on transition metals and alkali/alkaline element-doped NiO_x films.

The performances of PSCs have been significantly improved through various transition-metal-doped NiO_x, compared with those with pristine NiO_x. In terms of electrical properties, hole mobility and conductivity were increased, and the reduced roughness allowed the improvement of the morphology between NiO_x and perovskite layers. As an additional advantage, the energy barrier at the junction between NiO_x and perovskite can be reduced by fine tuning the work function of NiO_x. Through these merits, it is expected that the transition metal doping technique of NiO_x could be applied to other oxide-based HTLs (i.e., CuO, SnO₂, TiO₂).

3.2. Rare-Earth Metals Doping

Apart from the above-mentioned transition metals, rare-earth elements have been utilized as promising dopants for NiO_x HTLs. In general, rare-earth elements have been used to improve the magnetic and superconducting properties of metal oxide semiconductors.^[114] However, their partially filled 4*f* orbitals and vacant 5*d* orbitals exhibited better energy-level structures of NiO_x.^[115] Furthermore, its large transmission coefficient and higher optical bandgap improved the optical transparency of NiO_x without compromising its conductivity. The ionic radius of the rare-earth ion is greater than that of NiO_x, which induces more interstitial or substitutional sites. It exhibits donor-like behavior with the association of oxygen vacancies.^[116] Chen et al. improved the conductivity of the NiO_x HTL using various trivalent rare-earth ions such as Ce, Nd, Eu, Tb, and Yb as dopants.^[117] The results demonstrated that 3% europium (Eu) doping produced a smooth and compact NiO_x thin film even with high conductivity, and it was advantageous to grow the perovskite layer having larger grain size. Consequently, the carrier extraction property was enhanced and recombination was suppressed. The PCE of device was enhanced from 12.20% to 15.06%, which was a 23.4% increase. Subsequently, Goumri–Said et al. found that Eu doping on NiO_x would improve the transmittance and optical bandgap of NiO_x film within a certain doping limit. The Urbach energy level increased with the increase in Eu doping.^[118] Hu et al. studied the effect of yttrium (Y) doping on the NiO_x HTL for p–i–n PSCs. They added different concentrations (0–10%) of Y dopant to amorphous NiO_x, and their XPS results confirmed that the trivalent Y³⁺ was in NiO_x. The PSCs, built on 5% Y-doped NiO_x HTL, exhibited the superior PCE of 16.31% (J_{sc} of 23.82 mA, V_{oc} of 1.0 V, and FF of 68%), which was 27.62% enhancement compared with that of PSCs on undoped NiO_x HTL.^[119] Teo et al. incorporated lanthanum (La) into NiO_x for defect passivation purposes.^[120] The PL quenching and the decrement in charge transfer resistance (R_{ct}) (from 3100 Ω to 1200 Ω) confirmed that La effectively passivated the trap states in pristine NiO_x. In addition, La altered the VBM level of NiO_x, consequently enhancing its hole transportation property. Moreover, La doping drastically improved the stability of the devices, and 95% efficiency was retained even after 50 days. **Table 3** shows the performance of PSCs based on rare-earth element-doped NiO_x films.

The rare-earth metal doping method allowed the formation of dense and compact NiO_x thin films even with improved properties. The improved quality of NiO_x thin films increased the

Table 1. Summary of the device performances of transition metal-doped NiO_x thin film-based PSCs, transition metal elements, synthesis method of NiO_x, device configuration, cell area, open-circuit voltage, short-circuit current, FF, initial PCE, retained PCE, storage condition, storage time, and year of publication.

Dopant	Method	Device configuration	Area [cm ²]	V _{oc} [V]	J _{sc} [mA cm ⁻²]	FF [%]	Initial PCE [%]	Retained PCE [%]	Storage condition	Storage Time [days]	Year	Ref.
Cu	PLD	FTO/NiO _x /FA _{0.2} MA _{0.8} Pb _x Cl _{3-x} /PCBM/RhB/LiF/Ag	0.11	1.11	23.17	79.1	20.19	93.9	20% relative humidity (RH)/25 °C (w/o encapsulation)	30	2020	[97]
Co	Spin coating	FTO/NiO _x /CH ₃ NH ₃ PbI ₃ /PCBM/PEI/Ag	0.05	1.09	20.46	79.8	17.77	80.0	N ₂ -filled glove box (w/o encapsulation)	10.42	2020	[96]
Al	Spin coating	ITO/NiO _x /CH ₃ NH ₃ PbI ₃ /PCBM/Am-TiO ₂ /Ag	0.40	1.06	24.34	81.3	20.84	84.3	Glove box (w/o encapsulation)	72	2020	[99]
Cu	Spin coating	ITO/NiO _x /CH ₃ NH ₃ PbI ₃ /PCBM/Ag	0.05	1.03	21.24	72.5	15.88	N/A	N/A	N/A	2020	[170]
Fe	Spin coating	FTO/NiO _x /CH ₃ NH ₃ PbI ₃ /PCBM/BCP/Ag	0.04	1.0	19.21	84.5	17.61	N/A	N/A	N/A	2019	[101]
Co	Spin coating	ITO/NiO _x /CH ₃ NH ₃ PbI ₃ /PCBM/bis-C ₆₀ /Ag	0.01	1.04	22.97	74.0	17.52	94.0	N/A	30	2019	[110]
Y	Sol-gel	FTO/NiO _x /CH ₃ NH ₃ PbI ₃ /PCBM/Au	0.08	1.00	23.82	68.0	16.31	N/A	N/A	N/A	2018	[119]
Zn	Spin coating	ITO/NiO _x /CH ₃ NH ₃ PbI ₃ /PCBM/bis-C ₆₀ /Ag	0.11	1.03	21.84	61.0	13.72	N/A	N/A	N/A	2018	[100]
Ag	Spin coating	ITO/NiO _x /CH ₃ NH ₃ PbI ₃ /PCBM/BCP/Ag	0.40	1.07	19.42	79.0	16.42	80.0	30 ± 2% RH (w/o encapsulation)	30	2018	[98]
Co	Spin coating	ITO/NiO _x /CH ₃ NH ₃ PbI ₃ /PCBM/PEI/Ag	0.04	1.05	22.3	79.0	18.60	N/A	N/A	N/A	2018	[109]
Zn	Sol-gel	FTO/NiO _x /CH ₃ NH ₃ PbI ₃ /PCBM/BCP/Ag	0.03	1.10	22.8	78.0	19.60	90.0	Dry air	30	2018	[171]
Cu	Spin coating	FTO/NiO _x /CH ₃ NH ₃ PbI ₃ /PCBM/Ag	0.03	1.06	20.79	64.0	14.88	90.0	60% RH/30 °C (w/o encapsulation)	10	2018	[172]
Cu	Spin coating	ITO/NiO _x /CH ₃ NH ₃ PbI ₃ /C ₆₀ /BCP/Ag	0.08	1.12	22.28	81.2	20.26	95.0	50–60% RH/23 °C (with encapsulation)	41.7	2018	[102]
Cu	Sol-gel	FTO/NiO _x /mp-NiO _x /CH ₃ NH ₃ PbI ₃ /PCBM/Ag	0.06	1.11	21.58	82.0	19.62	94.0	30% RH/25 °C (w/o encapsulation)	41.7	2017	[173]
Cu	Combustion	ITO/NiO _x /Cysteine/CH ₃ NH ₃ PbI ₃ /PCBM/Bphen/Al	0.12	1.11	23.60	76.0	18.30	48.0	60% RH/25 °C (w/o encapsulation)	5	2017	[107]
Cu	Spin coating	ITO/NiO _x /CH ₃ NH ₃ PbI ₃ /PCBM/BCP/Ag	0.10	1.11	20.76	81.0	18.66	86.0	Ambient atmosphere/25 °C (w/o encapsulation)	30	2017	[174]
Cu	Spin coating	ITO/NiO _x /CH ₃ NH ₃ PbI _{3-x} Cl _x /PCBM/ZrAcac/Al	N/A	1.12	23.07	77.1	20.14	N/A	N/A	N/A	2017	[175]
Cu	Spin coating	ITO/NiO _x /CH ₃ NH ₃ PbI ₃ /PCBM/LiF/Al	N/A	1.04	18.10	75.5	14.20	N/A	N/A	N/A	2017	[176]
Cu	Sol-gel	ITO/UVO-NiO _x /CH ₃ NH ₃ PbI ₃ /PCBM/Al	N/A	1.02	17.10	71.0	12.20	N/A	N/A	N/A	2016	[104]
Co	Magnetron sputtering	FTO/NiO _x /CH ₃ NH ₃ PbI ₃ /PCPM/Ag	0.07	1.01	20.02	63.4	12.63	90.0	60% RH/30 °C (w/o encapsulation)	10	2012	[108]
Cu	Combustion	ITO/NiO _x /CH ₃ NH ₃ PbI ₃ /C ₆₀ /bis-C ₆₀ /Ag	0.03	1.05	22.23	76.0	17.74	N/A	N/A	N/A	2015	[78]
Cu	Sol-gel	ITO/NiO _x /CH ₃ NH ₃ PbI ₃ /PCPM/bis-C ₆₀ /Ag	0.03	1.11	19.01	73.0	15.40	90.0	Ambient air (w/o encapsulation)	10	2014	[177]

crystallinity and grain size of perovskite layer, resulting in enhanced PV parameters. Although this doping approach is not very suitable for commercialization due to the use of rare and expensive metals, it can be evaluated to broaden the insight into NiO_x doping mechanisms using various metal elements.

3.3. Multielements Codoping Strategy

The former section is about strategies, utilizing single element for NiO_x doping to improve its surface morphology, conductivity, and band alignment. However, this approach often reduces the transmittance of the thin film,^[121,122] degrading the

performances of p–i–n-structured PSCs.^[123] This can be improved by reducing the thickness of the film.^[108] However, the preparation of such an ultrathin film without defects like pinholes requires considerable expertise. Alternatively, the multi-component doping approach has been extensively investigated as an efficient way to improve its transmittance, and various codoping strategies were developed to enhance the performance of PSCs. Chen et al. demonstrated that Li and Mg codoping improved lattice stability due to the small difference in the ionic radii of Li (0.76 Å), Mg (0.71 Å), and Ni (0.69 Å).^[124] **Figure 13a** shows the schematic representation of Li- and Mg-codoped NiO_x-based PSC devices. Li and Mg codoping also enhanced the

Table 2. Summary of the device performances of alkali metal-doped NiO_x thin film-based PSCs, alkali metal elements, synthesis method of NiO_x, device configuration, cell area, open-circuit voltage, short-circuit current, FF, initial PCE, retained PCE, storage condition, storage time, and year of publication.

Dopant	Method	Device configuration	Area [cm ²]	V _{oc} [V]	J _{sc} [mA cm ⁻²]	FF [%]	Initial PCE [%]	Retained PCE [%]	Storage Condition	Storage time (days)	Year	Ref.
Li	Spin coating	ITO/NiO _x /CH ₃ NH ₃ PbI ₃ /PCBM/Ag	0.13	1.01	18.30	68.0	12.60	N/A	N/A	N/A	2019	[178]
K	Spin coating	FTO/NiO _x /Cs _{0.05} FA _{0.81} MA _{0.14} Pb(Br _{0.15} I _{0.85}) ₃ /PCBM/ITO/Ag	0.04	1.13	20.53	74.0	17.02	80.0	N ₂ -filled glove box (w/o encapsulation)	35	2019	[179]
Rb	Sol-gel	ITO/NiO _x /Cs _{0.1} FA _{0.7} MA _{0.2} I _{3-x} Br _x /PCBM/BCP/Ag	0.31	1.05	21.77	75.3	17.21	N/A	N/A	N/A	2019	[180]
Ba	Spin coating	FTO/NiO _x /CH ₃ NH ₃ PbI ₃ /PCBM/BCP/Ag	0.06	1.10	22.24	73.7	17.94	N/A	N/A	N/A	2019	[181]
Sr	Spin coating	FTO/NiO _x /CH ₃ NH ₃ PbI ₃ /PCBM/BCP/Ag	0.06	1.14	22.66	75.6	19.49	90.0	15% RH/25 °C (w/o encapsulation)	30	2019	[181]
Mg	Spin coating	FTO/NiO _x /CH ₃ NH ₃ PbI ₃ /PCBM/BCP/Ag	0.06	1.10	22.44	74.4	18.29	N/A	N/A	N/A	2019	[181]
Ca	Spin coating	FTO/NiO _x /CH ₃ NH ₃ PbI ₃ /PCBM/BCP/Ag	0.06	1.13	22.30	74.8	18.75	N/A	N/A	N/A	2019	[181]
Sr	Spin coating	FTO/NiO _x /(FA _{0.15} MA _{0.85})Pb(I _{0.95} Br _{0.05}) ₃ /PCBM/AgAl	N/A	1.11	22.73	79.4	20.06	60.0	18% RH (w/o encapsulation)	100	2018	[182]
Li	Sol-gel	ITO/NiO _x /CH ₃ NH ₃ PbI ₃ /PCBM/Ag	N/A	1.00	20.89	74.0	15.41	N/A	N/A	N/A	2018	[183]
Li	Sol-gel	FTO/NiO _x /CH ₃ NH ₃ PbI _{3-x} Cl _x /PCBM/Ag	N/A	1.12	21.79	74.0	18.06	N/A	N/A	N/A	2015	[184]
Mg	Sputtering	ITO/NiO _x /CH ₃ NH ₃ PbI ₃ /PCBM/ZnMgO/Al	0.10	1.08	21.30	79.0	18.20	90.0	50–70% RH/25 °C (with encapsulation)	25	2017	[88]
Li	Spin coating	ITO/NiO _x /CH ₃ NH ₃ PbI ₃ Cl _{3-x} /PCBM/Al	0.05	1.12	21.79	73.6	17.96	N/A	N/A	N/A	2017	[132]
Cs	Spin coating	FTO/NiO _x /CH ₃ NH ₃ PbI ₃ /PCBM/ZrAcac/Ag	0.01	1.12	21.77	79.3	19.35	98.0	Ar-filled glove box (w/o encapsulation)	70	2017	[185]
Li	PLD	ITO/NiO _x /CH ₃ NH ₃ PbI _{3-x} Cl _x /PCBM/Ag	0.07	1.05	22.80	64.2	15.51	86.5	Glove box (≈28 °C) (w/o encapsulation)	20	2017	[102]
Cs	Sol-gel	FTO/NiO _x /Cs _{0.05} [(FAPbI ₃) _{0.83} (MAPbBr ₃) _{0.17}] _{0.95} /PCBM/BCP/Ag	0.16	1.03	21.4	78.0	17.20	N/A	N/A	N/A	2017	[186]

Table 3. Summary of the device performance of rare-earth metal-doped NiO_x thin film-based PSCs, rare earth metal elements, synthesis method of NiO_x, device configuration, cell area, open-circuit voltage, short-circuit current, FF, initial PCE, retained PCE, storage condition, storage time, and year of publication.

Dopant	Method	Device configuration	Area [cm ²]	V _{oc} [V]	J _{sc} [mA cm ⁻²]	FF [%]	Initial PCE [%]	Retained PCE [%]	Storage condition	Storage time [days]	Year	Ref.
Ce	Spin coating	FTO/NiO _x /CH ₃ NH ₃ PbI ₃ /PCBM/Ag	0.10	1.03	21.60	58.6	12.97	N/A	N/A	N/A	2019	[117]
Nd	Spin coating	FTO/NiO _x /CH ₃ NH ₃ PbI ₃ /PCBM/Ag	0.10	0.94	19.37	70.6	12.86	N/A	N/A	N/A	2019	[117]
Eu	Spin coating	FTO/NiO _x /CH ₃ NH ₃ PbI ₃ /PCBM/Ag	0.10	1.03	21.96	66.6	15.06	97.0	25–55% RH/25–35 °C (with encapsulation)	10	2019	[117]
Yb	Spin coating	FTO/NiO _x /CH ₃ NH ₃ PbI ₃ /PCBM/Ag	0.10	0.99	21.58	64.1	13.70	N/A	N/A	N/A	2019	[117]
Tb	Spin coating	FTO/NiO _x /CH ₃ NH ₃ PbI ₃ /PCBM/Ag	0.10	0.98	20.08	69.0	13.58	N/A	N/A	N/A	2019	[117]
La	Spin coating	FTO/NiO _x /CH ₃ NH ₃ PbI ₃ /PCBM/BCP/Ag	0.08	1.02	20.25	73.0	15.03	95.0	Moisture-free desiccator (w/o encapsulation)	30	2018	[120]

electrical conductivity of NiO_x thin film by 10 times from 0.3 to 3 nA at 1 V bias, as shown in Figure 13d.^[124] Moreover, the carrier concentration improved from $2.66 \times 10^{17} \text{ cm}^{-3}$ (NiO_x) to $6.46 \times 10^{18} \text{ cm}^{-3}$ (Li_{0.05}Mg_{0.15}Ni_{0.8}O), obtained from the Hall effect measurement setup. Mg doping reduced the undesirable shift in the valence band due to Li doping. The large-area (1.02 cm²) PSC device showed 16.2% efficiency with superior stability.

Li and coworkers observed enhancement in electrical conductivity, hole mobility, surface smoothness, and work function with Li and Ag codoping strategy.^[125] The grain size of MAPbI₃, built on Li- and Ag-codoped NiO_x thin film, increased compared with

that of MAPbI₃, cast on pristine NiO_x, Li-doped NiO_x, and Ag-doped NiO_x thin films, as shown in Figure 13b. The crystal structures of pristine NiO_x and Li- and Ag-codoped NiO_x along with their DOS are shown in Figure 13c. The theoretically calculated DOS showed that Li- and Ag-codoped NiO_x had shallower acceptor levels than those of the pristine NiO_x, beneficial to the enhancement of hole concentration. The best efficiency of Li- and Ag-codoped NiO_x PSCs was 19.24% with 30 days of stability (95% retained) under 30% humidity condition.

Niu et al. investigated the effect of oxygen vacancy by annealing the LiMgNiO_x film in dry air and N₂ environment and found

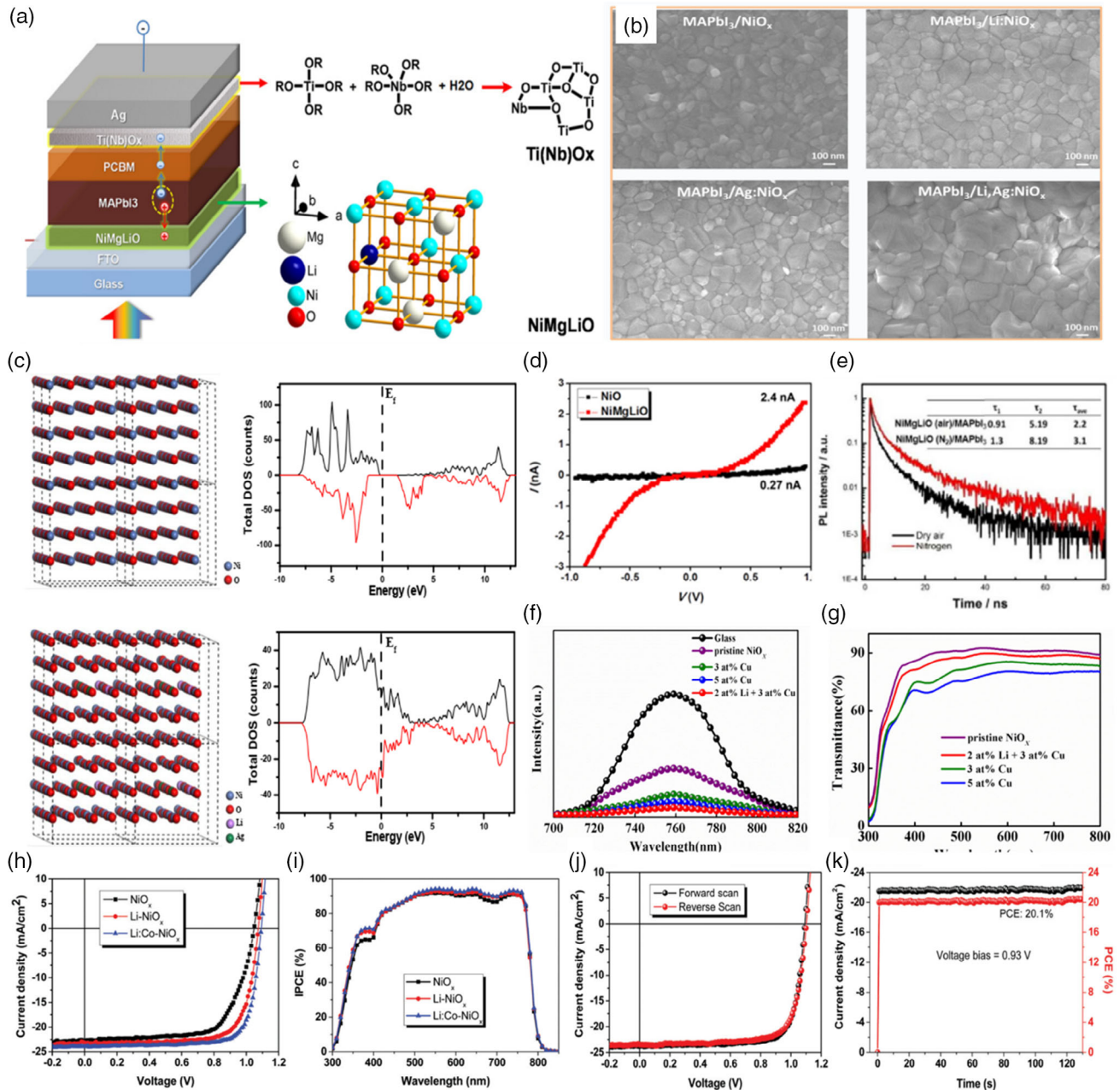


Figure 13. a) Schematic representation of PSCs and atomic arrangement of Li- and Mg-doped NiO_x. Reproduced with permission.^[124] Copyright 2015, American Association for the Advancement of Science. b) Top viewed SEM images of MAPbI₃ films deposited on the pristine NiO_x and Li/Ag-doped NiO_x. c) Atomic arrangements and DOS of pristine and Li- and Ag-doped NiO_x. Reproduced with permission.^[125] Copyright 2018, American Chemical Society. d) Electrical conductivity of pristine and Li- and Mg-doped NiO_x. Reproduced with permission.^[124] Copyright 2015, American Association for the Advancement of Science. e) Carrier lifetime of Li- and Mg-doped NiO_x in the presence of air and N₂ gas. Reproduced with permission.^[126] Copyright 2018, The Royal Society of Chemistry. f) PL spectrum of pristine, Cu, and Li- and Cu-doped NiO_x. Reproduced with permission.^[127] Copyright 2016, The Optical Society. g) Transmission spectrum of Cu and Li and Cu-doped NiO_x. Reproduced with permission.^[127] Copyright 2016, The Optical Society. h) *J*–*V* curve of pristine, Li, and Li- and Co-doped NiO_x-based solar cell. i) Incident photon-to-electron conversion efficiency of pristine, Li, and Li- and Co-doped NiO_x-based solar cell. j) Hysteresis curve of Li- and Co-doped NiO_x-based solar cell and k) stability analysis of Li- and Co-doped NiO_x-based solar cell. Reproduced with permission.^[128] Copyright 2020, Elsevier.

that the sample, prepared in dry air, had small energy difference between the VBM values of HTM and perovskite, beneficial to charge transfer.^[126] The average lifetime of the sample, prepared in dry air, was 2.2 ns, shorter than that of the sample, prepared in

nitrogen atmosphere (3.1 ns), as shown in Figure 13e, and this led to the efficient charge transfer between LiMgNiO_x and perovskite layer. The device fabricated on dry air-annealed LiMgNiO_x layer showed 19.2% efficiency with negligible hysteresis.

Another codoping approach with Li and Cu was reported by Wu and coworkers^[127] They found that the optimum doping concentrations of Li and Cu were 2% and 3%, respectively. The hole mobility of 2% Li- and 3% Cu-doped NiO_x film was shown to be 165.9 cm² V⁻¹ s⁻¹, much higher than that of 5% Cu single-element-doped NiO_x film (100.9 cm² V⁻¹ s⁻¹). The improvement in mobility enhanced the electrical conductivity, which led to the increment in the charge extraction capability of NiO_x film. PL quenching behaviors of perovskites cast on various HTMs in Figure 13f confirm the efficient charge extraction at the interface between the 2% Li- and 3% Cu-doped NiO_x and perovskite. The transmittance of 2% Li- and 3% Cu-doped NiO_x layer was also enhanced compared with that of 5% Cu-doped NiO_x (Figure 13g). Consequently, the 2% Li- and 3% Cu-doped NiO_x thin film-based PSC showed 14.53% PCE, which was around 25% higher than that of the pure Cu-doped NiO_x-based PSC.

Wang et al. reported Li and Co doping strategy, which could improve the properties of NiO_x layer.^[128] The efficiency of PSCs, fabricated on Li_{0.10}Co_{0.05}Ni_{0.85}O thin film, was 20.1%, superior to that of PSCs, prepared on any other codoped NiO_x thin films. *J*–*V* curves and EQE signals are shown in Figure 13h,i. The PSC devices operated without hysteresis are shown in Figure 13j,k. Recently, Li and Pb codoping strategy was also studied, and the PSC device with 17.02% efficiency, higher than that of PSCs on an undoped layer (15.4%), was reported.^[129] **Table 4** shows the performance of PSCs based on codoped element-added NiO_x films.

In addition to the monometal element doping methods, multi-metal element codoping methods have been also actively studied. Even if this method is slightly more complex, it has shown that the electrical and optical properties of the NiO_x thin films can be effectively controlled by changing the composition of each metal element. By adjusting the composition of metal elements, the oxygen vacancy state, which can tune the work function of NiO_x, can be changed efficiently. Therefore, designing multielements codoping strategy can be considered as a creative approach to improve the performances of PSCs.

3.4. Surface Modification of NiO_x

Surface modification is one of the widely utilized methods to modify the surface properties, electrical conductivity, morphology, and work function. As for NiO_x film, Ni²⁺ of the Ni atom vacancy is replaced by Ni³⁺, which creates the shallow acceptor level. This observation helps to understand the requirement of substitutional doping and thus the modification of the oxidation states of NiO_x film.^[126]

Surface contamination often reduces the work function of NiO_x thin film. UV–O₃ and O₂ plasma treatment have been widely utilized to remove those,^[130] but the property of the films is also modified with these processes. For instance, the work function at around 5.24–5.4 eV was reported after the UV–O₃ treatment,^[61,62] which was lower than that of the commonly reported value (4.8 eV).^[130] Moreover, these are not absolute values and strongly depend on the synthetic methods of NiO_x and perovskite thin films.^[131] Different from those, functionalization of NiO_x thin films with organic and hybrid materials has been investigated as an efficient, reproducible, and less synthesis-sensitive approach to improve the performances of the PSCs.^[35]

Organic molecules can be utilized to modify NiO_x thin film. It has been reported that F6TCNNQ extracted electrons from NiO_x due to its high electron affinity and used a strong connection with the surface of HTM.^[132] This ensured the stable growth of perovskite thin film on the organic molecule-doped NiO_x. Energy-level diagrams of NiO_x, organic layer, and perovskite are shown in **Figure 14a**. The energy-level differences between VBM and Fermi energy level significantly reduced from 0.58 to 0.29 eV after F6TCNNQ doping (Figure 14b). The work functions (VBM levels) of pristine and F6TCNNQ-included NiO_x film are 4.63 (5.21) and 5.07 (5.36) eV, respectively, as shown in Figure 14c–e, confirming the fast electron transfer from NiO_x to F6TCNNQ. The cross-sectional SEM image of the device, along with element mapping, is shown in Figure 14f. The maximum device efficiency, based on F6TCNNQ-doped NiO_x thin film, was 20.86% (Figure 14g) without hysteresis (Figure 14h,i).

Table 4. Summary of the device performance of co-doped NiO_x thin film-based PSCs, co-doped elements, synthesis method of NiO_x, device configuration, cell area, open-circuit voltage, short-circuit current, FF, initial PCE, retained PCE, storage condition, storage time, and year of publication.

Dopant	Method	Device configuration	Area [cm ²]	V _{oc} [V]	J _{sc} [mA cm ⁻²]	FF [%]	Initial PCE [%]	Retained PCE [%]	Storage condition	Storage time [days]	Year	Ref.
Li & Mg	Spray pyrolysis	FTO/NiO _x /CH ₃ NH ₃ PbI ₃ /PCBM/Ti(Nb)O _x /Ag	1.02	1.07	20.60	74.8	16.20	97.0	Dry cabinet < 20% RH (w/o encapsulation)	41.7	2015	[124]
Li & Mg	Spray pyrolysis	FTO/NiO _x /FA _{0.85} MA _{0.15} Pb(0.85Br _{0.15}) ₃ /PCBM//Ag	1.02	1.08	21.95	78.4	18.21	90.0	25% RH/25 °C (with encapsulation) AM 1.5 sunlight soaking	41.7	2016	[187]
Li & Cu	Spin coating	FTO/NiO _x /CH ₃ NH ₃ PbI ₃ /PCBM/Ag	N/A	0.97	20.28	71.8	14.04	N/A	N/A	N/A	2016	[127]
Li & Mg	Spin coating	FTO/NiO _x /CsFAMAPbI ₃ /PCBM/Ag	0.16	1.08	22.55	79.0	19.20	≈100.0	55% RH/25 °C (w/o encapsulation)	15	2018	[126]
Li & Ag	Spin coating	FTO/NiO _x /CH ₃ NH ₃ PbI ₃ /PCBM/BP/Ag	N/A	1.13	21.29	80.0	19.24	0.95	30 ± 2% RH/25 °C (w/o encapsulation)	30	2018	[125]
Li & Co	Spin coating	ITO/NiO _x /MAFAPbI ₃ /PCBM/BP/Ag	0.07	1.09	23.80	78.0	20.10	0.94	30–40% RH/25 °C (w/o encapsulation)	30	2019	[128]
Li & Pb	Spin coating	FTO/NiO _x /CH ₃ NH ₃ PbI ₃ /PCBM/BP/Ag	N/A	1.01	21.31	78.8	17.02	N/A	N/A	N/A	2020	[129]

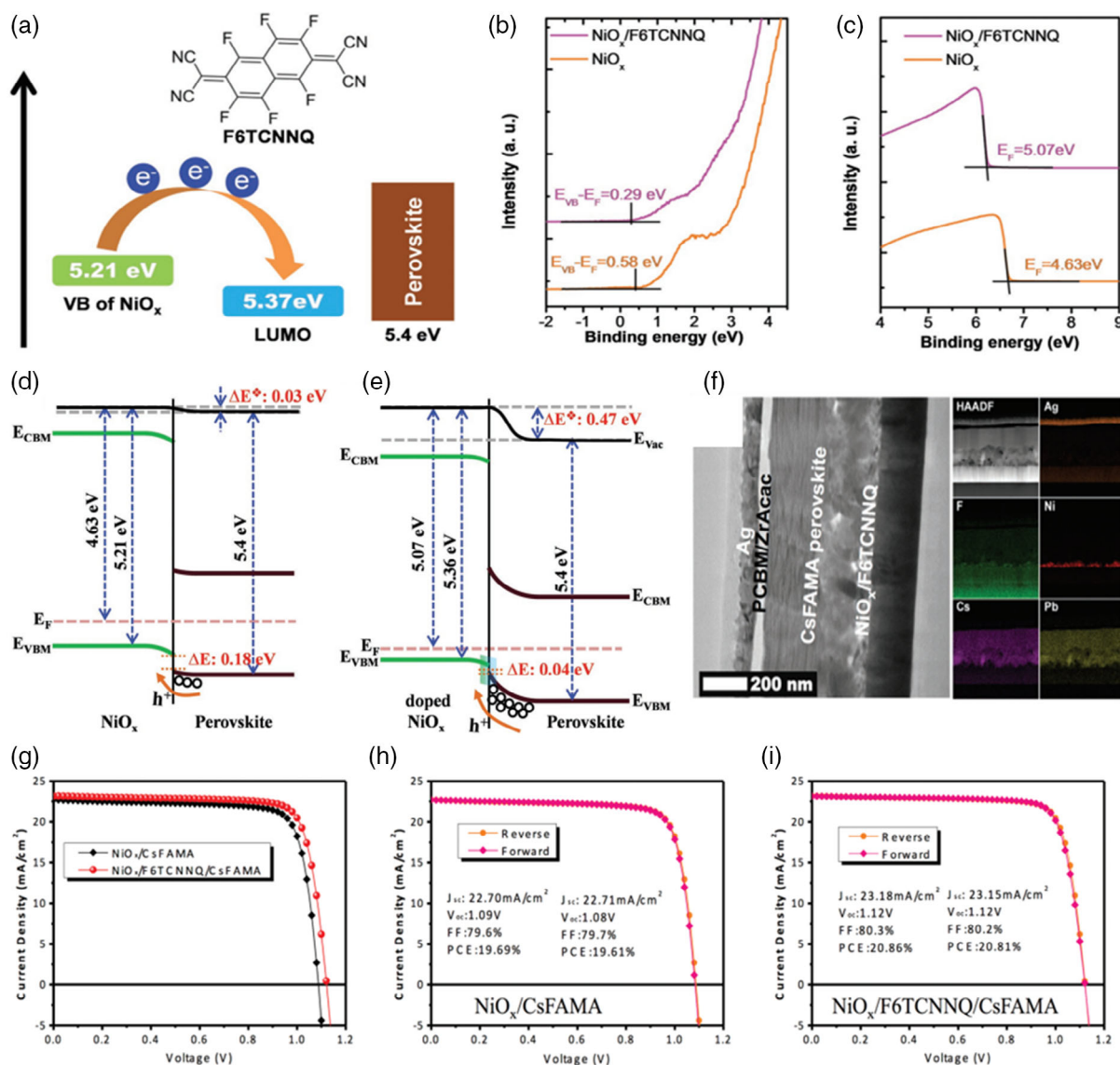


Figure 14. a) Energy band alignment of solar cell along with the chemical structure of F6TCNNQ. b) Valence band spectra of NiO_x and NiO_x/F6TCNNQ thin film. c) UPS spectrum of NiO_x and NiO_x/F6TCNNQ thin film. d) Band bending of NiO_x thin film-based solar cell. e) Band bending of NiO_x/F6TCNNQ thin film-based solar cell. f) SEM image and elemental mapping of NiO_x/F6TCNNQ thin film-based solar cell. g) Comparison of PCE of NiO_x and NiO_x/F6TCNNQ thin film-based solar cell. h) Hysteresis curve of NiO_x thin film-based solar cell and i) hysteresis curve of NiO_x/F6TCNNQ thin film-based solar cell. Reproduced with permission.^[132] Copyright 2018, WILEY-VCH.

Approaches to graft self-assembled monolayers on NiO_x surface by forming bonds through amines,^[133] carboxylates,^[134] and thiols^[107] with phosphonic acid have been introduced. The functionalization of NiO_x with the organic monolayer improved surface chemistry, and it was beneficial to grow defect-free absorber layer.^[35] It was also advantageous to stabilize the interface between NiO_x and perovskite and control their work functions for improving the performances of PSCs. Zhang et al. modified the NiO_x film with polymeric PTAA, and this could reduce the charge recombination at the interface between perovskite and PTAA/NiO_x due to gradient band alignment.^[135] The calculated trap densities on NiO_x and PTAA/NiO_x films were 1.06×10^{16} and $6.58 \times 10^{15} \text{ cm}^{-3}$, respectively, and the

perovskite layer on PTAA/NiO_x film had better quality with larger grain size. A similar effect was reported by the alkali halides such as NaCl^[136] and KCl.^[137]

Diethanolamine (DEA) monolayer was also utilized to modify NiO_x, which improved the surface morphology of the perovskite layer, but it does not affect the work function, and thus V_{oc} of PSCs remained almost the same.^[138] He et al. used cysteine and mercaptoethylamine (Merc) to modify the CuNiO_x surface.^[107] Carboxyl group or amine chlorate interacted with CuNiO_x, and the sulfhydryl group worked as the anchoring group, which formed the Ni-S bond. The remaining -NH₃ groups were exposed for the interaction with perovskite materials. Additional carboxyl groups helped to improve the work function

of the HTL. The performances of the devices were improved to 18.3% due to the highly crystallized film and favorable interfacial contact, enhancing their J_{sc} and V_{oc} . Tavakoli and coworkers used poly [(9,9-bis(3'-((*N,N*-dimethyl)-*N*-ethylammonium)-propyl)-2,7-fluorene)-alt-2,7-(9,9-dioctylfluorene)] dibromide (PFN-P2) to modify the NiO_x film.^[139] By introducing PFN-P2 to NiO_x , surface roughness reduced from 13 to 6 nm, which reduced recombination and enhanced charge transfer at the interface between NiO_x and perovskite. About 20.5% efficiency was achieved after modifying the NiO_x thin film with PFN-P2.

We newly synthesized a series of triphenylamine-imidazole (TPI) derivatives having different numbers of methoxy units from 2 to 6 (TPI-2MEO, TPI-4MEO, and TPI-6MEO) for passivating unsaturated bonds of NiO_x and defects in perovskite, simultaneously.^[140] The chemical structures of the TPis with different numbers of methoxy unit are shown in **Figure 15a**. IR spectrum of TPI-6MEO/ NiO_x showed an additional Ni–N vibrational peak at around 526 cm^{-1} , which was not observed from the pristine NiO_x . This confirmed that N atoms of organic molecules formed covalent bonds with Ni atoms of NiO_x layer,

saturation oxygen vacancy. Moreover, Pb–O stretching peaks in Raman spectrum of TPI-6MEO/perovskite also represented the passivation of Pb^{2+} defects in perovskite by methoxy units in TPis. In addition, the HOMO levels of molecules were deepened to have better alignment with the VBM of perovskite as the number of methoxy units increased (Figure 15b). The cross-sectional SEM image of the device and top-view SEM image of perovskite are shown in Figure 15e,f, respectively. After passivating defects in both NiO_x and perovskite with organic functional groups, steady-state (Figure 15g) and time-resolved PL (Figure 15i) of perovskite were efficiently quenched, and the absorbance of perovskite was enhanced. Consequently, the device performance was improved with TPI-6MEO, which reached 18.42% (Figure 15c). The PSC devices did not show hysteretic behavior (Figure 15d) and represented superior stability (Figure 15j). **Table 5** shows the performances of PSCs, fabricated on the surface-functionalized NiO_x thin films.

The solution-based processes are generally utilized to form NiO_x thin films due to their simplicity and cost-effectiveness. However, the NiO_x thin films formed by these methods often

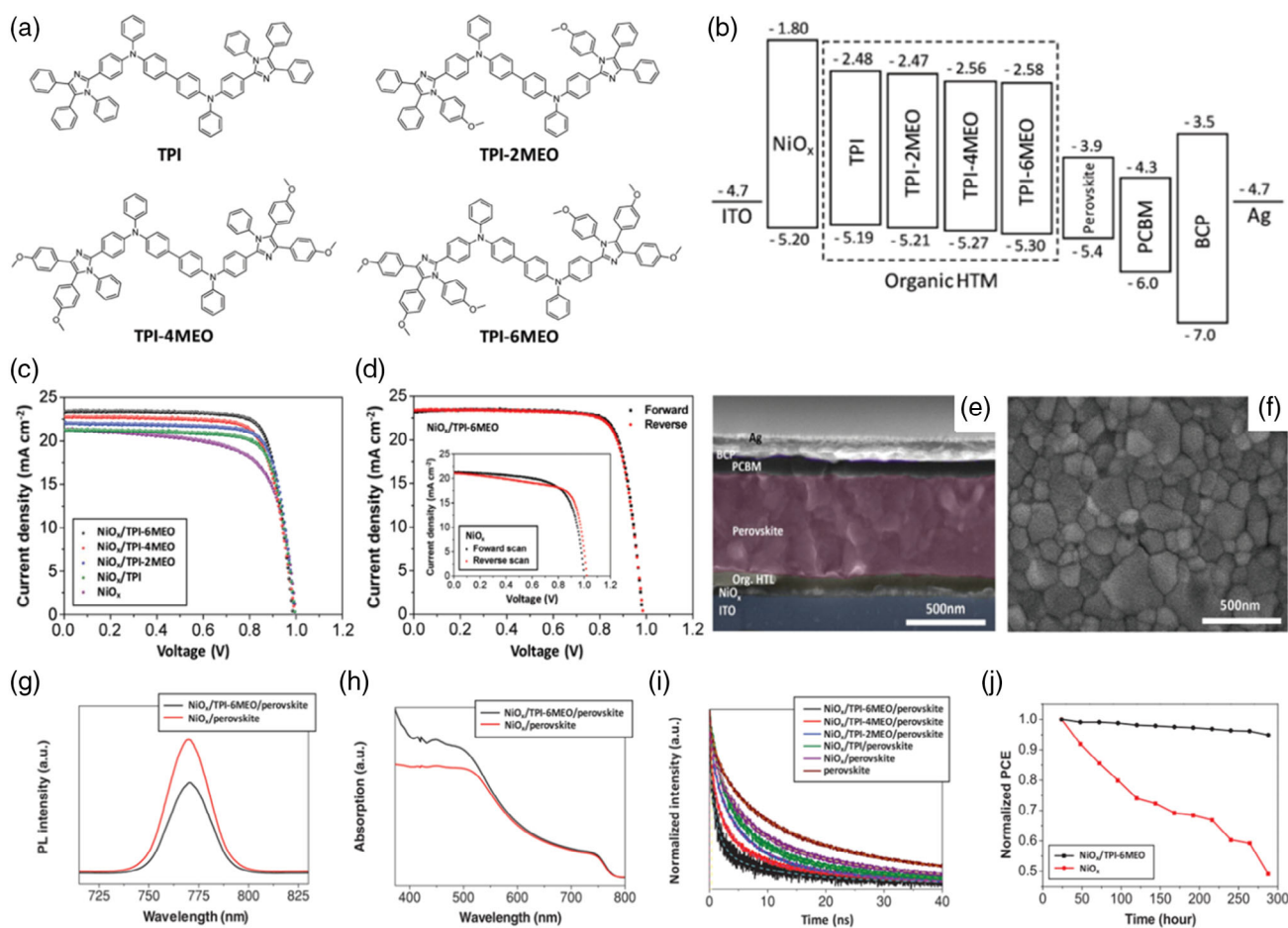


Figure 15. a) Chemical structure of methoxy-functionalized TPI. b) Energy band alignment of different layers of solar cells. c) J – V curve of pristine and methoxy-functionalized TPI NiO_x thin film, d) Hysteresis curve of pure NiO_x and NiO_x /TPI-6MEO-based solar cell. e) SEM image of different layers of solar cells. f) Surface morphology of perovskite layer. g) PL spectrum of NiO_x and NiO_x /TPI-6MEO thin film. h) Absorption spectrum of NiO_x and NiO_x /TPI-6MEO thin film. i) Carrier lifetime of pristine and methoxy-functionalized TPI NiO_x thin film and j) comparison of stability of NiO_x and NiO_x /TPI-6MEO thin film-based solar cell. Reproduced under the terms of a CC-BY license.^[140] The Authors, published by Copyright 2019, WILEY-VCH.

Table 5. Summary of the device performance of surface functionalized NiO_x thin film-based PSCs, surface functionalized materials, synthesis method of NiO_x, device configuration, cell area, open-circuit voltage, short-circuit current, FF, initial PCE, retained PCE, storage condition, storage time and year of publication.

Dopant	Method	Device configuration	Area [cm ²]	V _{oc} [V]	J _{sc} [mA cm ⁻²]	FF [%]	Initial PCE [%]	Retained PCE [%]	Storage condition	Storage time [days]	Year	Ref.
UV	Spin coating	ITO/NiO _x /CH ₃ NH ₃ PbI ₃ /PCBM/Al	0.07	1.05	15.40	47.0	7.6	N/A	N/A	N/A	2014	[61]
UV-O ₃	Spin coating	ITO/NiO _x /CH ₃ NH ₃ PbI ₃ /PCBM/BCP/Al	0.06	0.92	12.43	68.0	7.8	N/A	N/A	N/A	2014	[62]
PVP/UV-O ₃	Spin coating	ITO/ P-UVO-NiO _x /CH ₃ NH ₃ PbI ₃ /PCBM/C ₆₀ /BCP/Al	N/A	1.04	20.10	52.1	10.9	N/A	N/A	N/A	2015	[188]
DEA	Sol-gel	FTO/NiO _x (DEA)/CH ₃ NH ₃ Pb I _{3-x} Cl _x /PCBM/PN ₄ N/Ag	0.10	0.95	20.90	80.0	15.9	N/A	N/A	N/A	2016	[60]
SAMs	Spin coating	ITO/NiO _x (SAM)/CH ₃ NH ₃ PbI ₃ /PCBM/bis-C ₆₀ /Ag	0.10	1.11	21.70	76.3	18.4	80.0	30% RH/25 °C (w/o encapsulation)	15	2017	[189]
DEA	Sol-gel	ITO/NiO _x /DEA/CH ₃ NH ₃ PbI ₃ /C ₆₀ (CH ₂)(Ind)/Ag	0.16	1.13	20.40	80.0	18.1	70.0	45% RH/25 °C (w/o encapsulation)	10	2017	[138]
cysteine	Spin coating	ITO/CuNiO _x /CH ₃ NH ₃ PbI ₃ /PCBM/Bphen/Al	N/A	1.11	23.60	70.0	18.3	N/A	N/A	N/A	2018	[107]
Merc	Spin coating	ITO/CuNiO _x /CH ₃ NH ₃ PbI ₃ /PCBM/Bphen/Al	N/A	1.07	22.30	64.0	15.3	N/A	N/A	N/A	2018	[107]
PhNa-IT	Spin coating	ITO/CuNiO _x /CH ₃ NH ₃ PbI ₃ /PCBM/Ag	0.12	1.03	21.40	77.1	17.0	0.75	30–40% RH/20–30 °C (w/o encapsulation)	11	2018	[190]
PTAA	Spin coating	FTO/NiO _x /FA _{1-x} MA _x Pb _{(3-y)Br_y} /PCBM/BCP/Au	N/A	1.02	20.80	78.3	16.7	N/A	N/A	N/A	2018	[135]
FDA	Spin coating	ITO/NiO _x /CH ₃ NH ₃ PbI ₃ /PCBM/AgAl alloy	N/A	1.04	22.55	76.2	17.59	N/A	N/A	N/A	2018	[134]
F6TCNNQ	Spin coating	ITO/NiO _x /C ₅₀ 0.05(FA _{0.85} MA _{0.15}) _{0.95} Pb(I _{0.85} Br _{0.15}) ₃ /PCBM/ZrAcacAg	N/A	1.12	23.18	80.3	20.8	N/A	N/A	N/A	2018	[132]
PFN-P2	Spin coating	ITO/NiO _x /C ₅₀ 0.05(FA _{0.85} MA _{0.15}) _{0.95} Pb(I _{0.85} Br _{0.15}) ₃ /C ₆₀ /BCP/Ag	N/A	1.13	23.33	77.6	20.5	0.86	N ₂ environment/25 °C AM 1.5 sunlight soaking (w/o encapsulation)	12.5	2019	[139]
UV-O ₃	ECD	FTO/NiO _x /CH ₃ NH ₃ PbI ₃ /PCBM/BCP/Ag	0.25	1.14	23.70	80.4	21.7	N/A	N/A	N/A	2019	[58]
Na:NaCl	Spin coating	ITO/NiO _x /C ₅₀ 0.05(FA _{0.83} MA _{0.17}) _{0.95} Pb(I _{0.83} Br _{0.17}) ₃ /C ₆₀ /BCP/Cu	0.16	1.09	21.20	74.0	17.1	N/A	N/A	N/A	2019	[136]
KCl	Spin coating	ITO/NiO _x /C ₅₀ 0.05(FA _{0.85} MA _{0.15}) _{0.95} Pb(I _{0.85} Br _{0.15}) ₃ /PCBM/ZrAcac/Ag	0.1	1.15	22.90	79.5	20.9	0.95	N ₂ -filled glove box (w/o encapsulation)	150	2019	[137]
TPI	Spin coating	ITO/NiO _x /CH ₃ NH ₃ PbI ₃ /PCBM/BCP/Ag	N/A	0.99	21.30	75.0	15.9	N/A	N/A	N/A	2019	[140]
TPI-2MeO	Spin coating	ITO/NiO _x /CH ₃ NH ₃ PbI ₃ /PCBM/BCP/Ag	N/A	0.99	22.01	76.0	16.5	N/A	N/A	N/A	2019	[140]
TPI-4MeO	Spin coating	ITO/NiO _x /CH ₃ NH ₃ PbI ₃ /PCBM/BCP/Ag	N/A	0.99	22.80	78.0	17.6	N/A	N/A	N/A	2019	[140]
TPI-6MeO	Spin coating	ITO/NiO _x /CH ₃ NH ₃ PbI ₃ /PCBM/BCP/Ag	N/A	0.98	23.30	81.0	18.4	0.85	N ₂ -filled glove box (w/o encapsulation)	12.5	2019	[140]
n-Butylamine	Spin coating	FTO/s-NiO _x /CH ₃ NH ₃ PbI ₃ /C ₆₀ /BCP/Ag	N/A	1.08	22.80	77.9	18.9	N/A	N/A	N/A	2019	[133]
TMAH	Spin coating	ITO/NiO _x /CH ₃ NH ₃ PbI ₃ /PCBM/Bis-C ₆₀ /Ag	N/A	1.08	21.90	72.0	17.0	0.40	Ambient air (w/o encapsulation)	96	2019	[191]
Air	Spin coating	FTO/NiO _x /CH ₃ NH ₃ PbI ₃ /PCBM/BCP/Ag	N/A	1.01	19.76	78.0	15.7	N/A	N/A	N/A	2019	[58]
O ₂	Spin coating	FTO/NiO _x /CH ₃ NH ₃ PbI ₃ /PCBM/BCP/Ag	N/A	1.02	19.45	75.0	14.9	N/A	N/A	N/A	2019	[58]
N ₂	Spin coating	FTO/NiO _x /CH ₃ NH ₃ PbI ₃ /PCBM/BCP/Ag	N/A	0.97	15.55	73.0	11.1	N/A	N/A	N/A	2019	[58]
Ar	Spin coating	FTO/NiO _x /CH ₃ NH ₃ PbI ₃ /PCBM/BCP/Ag	N/A	0.98	14.84	72.0	10.5	N/A	N/A	N/A	2019	[58]
CsBr	Spin coating	ITO/NiO _x /CsBr/FA _x MA _{1-x} Pb _{3-y} Cl _y /PCBM/BCP/Ag	N/A	1.09	23.50	75.1	19.2	0.82	30% RH/25 °C (w/o encapsulation)	37.5	2020	[192]

Table 5. Continued.

Dopant	Method	Device configuration	Area [cm ²]	V _{oc} [V]	J _{sc} [mA cm ⁻²]	FF [%]	Initial PCE [%]	Retained PCE [%]	Storage condition	Storage time [days]	Year	Ref.
Ethylphosphonic acid	Spin coating	ITO/NiO _x / Cs _{0.1} FA _{0.7} MA _{0.2} Pb(I _{0.75} Br _{0.25}) ₃ /PCBM/ BCP/Ag	N/A	1.03	19.50	65.0	13.0	0.50	Inert gas/75 °C Under sulfur plasma lamp irradiation 100 mW cm ⁻² (w/o encapsulation)	0.51	2020	[193]
4-Bromo benzoic Acid	Spin coating	ITO/NiO _x / Cs _{0.1} FA _{0.7} MA _{0.2} Pb(I _{0.75} Br _{0.25}) ₃ /PCBM/ BCP/Ag	N/A	0.99	17.70	72.0	12.6	0.50	Inert gas/75 °C Under sulfur plasma lamp irradiation 100 mW cm ⁻² (w/o encapsulation)	0.55	2020	[193]
Adenine	Spin coating	FTO/NiO _x /CH ₃ NH ₃ PbI ₃ /PCBM/PEI/Ag	N/A	1.06	22.90	77.7	18.96	0.90	50–60 RH/25 °C (w/o encapsulation)	25	2020	[194]
DPI	Spin coating	ITO/NiO _x /CH ₃ NH ₃ PbI ₃ /PCBM/BCP/Ag	N/A	1.04	22.90	78.0	18.6	N/A	N/A	N/A	2020	[195]
DNI	Spin coating	ITO/NiO _x /CH ₃ NH ₃ PbI ₃ /PCBM/BCP/Ag	N/A	1.09	23.80	78.0	20.30	0.90	Ambient air/25 °C AM 1.5 sunlight soaking (50 nm Al ₂ O ₃ encapsulation)	20.8	2020	[195]

have rough and uneven morphologies. To overcome this drawback, various studies have been conducted, which especially focused on surface modification. Among these studies, the research works on dual-functional organic materials, which can not only alleviate the roughness of NiO_x thin films but also passivate the defects of perovskite layer, have shown meaningful results. It has led to the establishment of an important concept of p-type organic material design suitable for PSCs.

4. Applications of NiO_x Thin Film to Perovskite-Based Tandem Solar Cells

Multijunction solar cells, which consist of multiple light-absorbing materials having dissimilar bandgaps, have shown prospectives in their PCEs beyond the Shockley–Queisser (S–Q) efficiency limit (single junction based), due to their absorption in the wide wavelength range. From the theoretical calculation, ≈46%, ≈50%, and ≈65% efficiencies were estimated from double-junction, triple-junction, and infinite-junction cells, respectively.^[141–143] The PSC is one of the best suitable candidates for the subcell of multijunction structures because of its exceptional properties like tunable bandgap, high structure tolerance, reducing the lattice mismatch at the interface, and high-defect tolerable limit, that originate from its intrinsic defects, mainly lying at the shallow level of valance band and conduction band.^[144] Moreover, long electron–hole diffusion lengths (>1 μm) and minority carrier lifetime (>1 μs) are advantageous for high carrier mobility,^[145] and its high absorption coefficient (1.5 × 10⁴ cm⁻¹ at 550 nm) is beneficial to reduce its material cost.^[146] As a partner of PSCs in double-junction tandem solar cell (TSC) structures, perovskite having different bandgaps, silicon (E_g = ≈1.12 eV) and copper indium gallium selenide (E_g = ≈1.1 eV), have been widely investigated, and a tandem cell built on a compound semiconductor gallium arsenide

(GaAs) was recently demonstrated by our research group.^[147–149] In this section, we especially focus on the TSC devices, which are composed of NiO_x-based PSCs, and the role of NiO_x in those TSCs will be discussed.

4.1. Perovskite/Si Tandem Solar Cells

Silicon is one of the most widely studied materials as a photoabsorber of bottom cells, because it has suitable bandgap, stability, huge market shares, and low manufacturing cost at the industrial scale.^[150,151] The maximum efficiency of Si-based solar cell, reported until now (26.7%), is close to its theoretical efficiency limit (about 29%), and thus to further improve its performance is challenging.^[152–154] In this context, the TSC architecture, which integrates the emerging PSCs as a top cell on the Si bottom cell, has brought a new opportunity that can enhance the efficiency of Si solar cell. This approach is also considered as one of the fastest routes to commercialize the PSC technology.^[155]

The maximum efficiency of perovskite/Si TSCs was 29.1% in 2020, which is higher than that of each Si and PSC,^[141,156] and, recently, even perovskite/perovskite/Si triple-junction solar cells were also demonstrated for optimal light management.^[157] The perovskite/perovskite double junction was built on a textured crystalline silicon at the bottom, designed for enhancing light trapping and minimizing light reflection; a high V_{oc} of 2.69 V was achieved. In this structure, 2,2',7,7'-tetra(N,N-di-tolyl) amino-9,9-spiro-bifluorene (spiro-TTB) was thermally deposited as HTL of the middle cell, but it cannot be utilized as an HTL of the top cell. To form a perovskite layer, cesium bromide (CsBr) and lead iodide (PbI₂) were coevaporated as a template layer on spiro-TTB layer, and then formamidinium iodide (FAI) solution was spin coated on the template, which was followed by thermal annealing for the perovskite crystal structure formation. Because the spiro-TTB layer was shown to dewet the transparent

conductive oxides during the annealing of the perovskite, 30 nm-thick NiO_x, deposited by the sputtering process, was utilized as an HTL of the top cell. This is due to the advantage of NiO_x that can form a stable and uniform layer even on the textured structure by properly selecting the deposition method.

4.2. Perovskite/CIGS Tandem Solar Cells

Other than Si, copper indium gallium diselenide (CIGS) has been widely investigated as a tandem partner of perovskite due to its suitable bandgap, high absorption coefficient for bottom cell, and high efficiency. In addition, the bandgap of CIGS is tunable in the range of 1.00–1.70 eV by modulation of the [Ga]/([Ga]+[In]) ratios.^[158] The maximum reported efficiency of CIGS solar cell is 23.35% along with high stability and cost-effectiveness.^[159] Both perovskite and CIGS layers can be prepared in a thin-film format, and thus perovskite/CIGS TSCs are feasible to the flexible solar cell, which has potential in building integrated PVs and mobile devices.^[160,161]

Jost et al. demonstrated a perovskite/CIGS TSC, of which a perovskite top cell was fabricated on a rough CIGS bottom cell.^[162] To avoid potential shunting due to the rough surface of CIGS, an ultrathin and uniform NiO_x layer is formed by ALD method on the front contact of the CIGS cell. The uniformly covered ALD-NiO_x prevented direct contact between perovskite and ZnO:Al. In addition, PTAA layer was introduced on the interface between NiO_x and perovskite to reduce the interface recombination losses by forming organic/inorganic bilayer-type HTLs, as explained in the cases of single-junction PSCs earlier.

4.3. Perovskite/GaAs Tandem Solar Cells

III–V compound semiconductors (e.g., GaAs) have various advantages over the conventional c-Si such as low-light performance, high efficiency, and small temperature coefficient,^[163,164] but their high production cost has limited their commercialization. Recently, we first demonstrated perovskite/GaAs TSCs, in which the conventional InGaP top cell was replaced with wide-bandgap (>1.82 eV) perovskite PV cells.^[165] For this purpose, a solvent-evaporation-controlled process that could provide a light-stable uniform wide-bandgap perovskite was newly developed. One of the main advantages of this TSC approach is that it can improve the usability of compound semiconductor-based PV technology with enhanced performance without significant cost increase for the applications, in which lightweight and flexibility are essential. To construct a PSC structure on the flexible bottom cell, solution-processible NiO_x NP HTL, prepared by the solvothermal method, was utilized for preventing the thermal degradation of the bottom cell.

4.4. All-Perovskite Tandem Solar Cells

Because bandgaps of perovskites can be easily tuned by controlling stoichiometries of components, all-perovskite TSCs, composed of perovskites having different bandgaps, have been extensively investigated. Especially, this approach is beneficial to realize high-performance TSCs with low manufacturing cost on flexible substrates.^[166,167] The highest PCEs of all-perovskite

TSCs, reported until now, are 25.6% and 24.2% for 0.049 and 1 cm², respectively,^[168] and the solution-processed NiO_x nanocrystal film was utilized as HTL of the wide-bandgap perovskite bottom cell of the TSC. The surface of NiO_x thin film was further modified with a spin-cast ultrathin (≈5 nm) organic layer, which was a thermally cross-linkable small molecule, N4,N4'-di(naphtalen-1-yl)-N4,N4'-bis(4-vinylphenyl)biphenyl-4,4'-diamine (VNPB), and this modification increased the V_{oc} of solar cell by ≈30 mV due to faster hole extraction and reduced interfacial nonradiative recombination. In addition, the VNPB could change the characteristics of NiO_x surface, which resulted in a more uniform perovskite layer on VNPB-modified NiO_x thin film. Meanwhile, a solution-processed all-perovskite triple-junction solar cell with V_{oc} of 2.8 V was also demonstrated.^[169] In this architecture, although NiO_x/PTAA bilayer was utilized to reduce the roughness of NiO_x in middle cell, severe V_{oc} loss was observed due to the roughness of the front subcell. To overcome this issue, conformal coating of HTL of middle cell on the rough surface of front subcell by sputtering, ALD, addition of self-assembled monolayers, and evaporation was suggested.

5. Conclusion and Future Outlook

In this Review, we reviewed the approaches to prepare high-performance NiO_x thin films for p–i–n-structured PSC devices, in which contents are mainly about 1) their synthetic methods including both solution- and vacuum-assisted processes, 2) modification of their properties with dopants and functional materials, and 3) application of NiO_x thin films to perovskite TSCs.

In general, NiO_x has various potential advantages as HTM of PSCs compared with other inorganic and organic HTMs: a well-aligned energy band with VBM of perovskite absorbers, fairly high electrical conductivity with proper hole mobility, high transmittance, low-temperature processibility, and cost-effectiveness. However, it also has shortcomings such as poor morphology, especially severe in solution-processed thin films. In planar p–i–n-structured PSCs, the properties of HTMs as the bottom layer have a profound effect on the quality of following perovskite layer. To figure out this issue, a variety of methods (i.e., solvothermal, combustion, PLD, e-beam, and ALD) have been applied to fabricate more denser, compact, and highly crystallized NiO_x thin films.

For further strengthening its merits, diverse methods such as doping of various types of metals (i.e., transition metals, alkali metals, alkaline metals, rare earth metals, and multimetals) and functionalization using organic materials have been widely studied. Among these, external doping significantly influences its optical and electrical properties by modifying its stoichiometry, oxidation states, and band structure and thus, enhancement in conductivity, transmittance, and work function. Those doping elements also affect structural properties, which improve the surface morphology and passivate the trap states. As for the surface functionalization with organic materials, the defects can be suppressed and its optical and electrical properties can be improved toward high-performance and stable planar PSCs. Those molecules behave as anchoring agents and form covalent bonds with the unsaturated atoms, decreasing the defect density at the

interface between NiO_x and perovskite, which can enhance the carrier extraction and blocking capability.

NiO_x is an efficient and cost-effective material with high stability, but NiO_x-based PSCs have various limitations to achieve high efficiency. As approaches to go beyond these limitations, we summarized various advanced fabrication and modification strategies here to resolve its disadvantages and further enhance its merits as a high-performance HTM of planar PSCs. Based on this Review, we suggest several strategies and outlooks for the application of NiO_x to the PSC devices. First, an appropriate synthesis method should be selected after considering device area and uniformity, required for the devices. A solution-based spin-casting process at low temperatures is commonly utilized to form NiO_x thin film, but it is unsuitable for large-area devices and often induces nonuniform surface. As discussed in this Review, various physical and chemical deposition methods such as electrodeposition, PLD, e-beam deposition, ALD, and sputtering deposition can be also applied to fabricate high-quality NiO_x thin films on large-area devices.

Second, the strategies to modify the properties of NiO_x should be considered. One of the most crucial goals of the solar cell devices is to produce higher efficiency under the same light environment. To achieve this goal, we can apply various approaches such as doping of HTL, passivation of perovskite layer through functional materials, and stabilization of the interface between HTL and perovskite. Especially for NiO_x HTLs, doping could be an efficient way that can dramatically enhance the efficiency of PSCs by increasing its conductivity as well as adjusting its energy level. Therefore, it is essential to optimize the type and concentration of the dopant after considering the characteristics of pristine NiO_x and the composition of perovskite. A bilayer-type HTL, composed of inorganic NiO_x and p-type organic semiconductor, could be an effective approach for improving the PV parameters of the device. Organic materials could improve the morphology of NiO_x and their functional groups could be utilized for passivating defects of perovskite such as undercoordinated Pb²⁺ and halide vacancies. To maximize these effects, the design of organic materials and their application to an interface between inorganic HTL and perovskite should be carefully considered.

NiO_x is a promising material for HTLs of PSCs in terms of efficiency, stability, and economics. Due to its relatively simple structure, it is also convenient to synthesize and dope, compared with other types of HTLs. Especially, this is feasible for multijunction PSCs, which are expected as one of the fastest routes to commercialize PSC technology. From this point of view, we believe that the application of NiO_x layer to solar cell devices could be close to commercialization. To go a step further, a future study should be focused on not only the improvement of device efficiency but also the optimization of its parameters in thin-film format for the mass production of flexible PSCs.

Acknowledgements

This work was supported by the National Research Foundation of Korea (NRF) grant funded by the Korea government (MSIT) (2020R1A2C2010342).

Conflict of Interest

The authors declare no conflict of interest.

Keywords

hole transport materials, inorganic materials, nickel oxide, perovskite solar cells, processing methods

Received: December 8, 2020

Revised: April 8, 2021

Published online: June 25, 2021

- [1] F. Birol, World Energy Outlook 2019, <https://www.iea.org/reports/world-energy-outlook-2019#electricity-demand-growth> (accessed: November 2019).
- [2] N. S. Lewis, in *Workshop for Basic Research Needs for Solar Energy Utilization*, Maryland, **2005**.
- [3] M. Green, E. Dunlop, J. Hohl-Ebinger, M. Yoshita, N. Kopidakis, X. Hao, *Prog. Photovolt. Res. Appl.* **2020**, *28*, 629.
- [4] S. Almosni, A. Delamarre, Z. Jehl, D. Suchet, L. Cojocar, M. Giteau, B. Behaghel, A. Julian, C. Ibrahim, L. Tetry, H. Wang, T. Kubo, S. Uchida, H. Segawa, N. Miyashita, R. Tamaki, Y. Shoji, K. Yoshida, N. Ahsan, K. Watanabe, T. Inoue, M. Sugiyama, Y. Nakano, T. Hamamura, T. Toupance, C. Olivier, S. Chambon, L. Vignau, C. Geffroy, E. Cloutet, et al., *Sci. Technol. Adv. Mater.* **2018**, *19*, 336.
- [5] G. Richhariya, A. Kumar, P. Tekasakul, B. Gupta, *Renew. Sustain. Energy Rev.* **2017**, *69*, 705.
- [6] The National Renewable Energy Laboratory is a national laboratory of the U.S. Department of Energy, NREL best research-cell efficiencies chart, <https://www.nrel.gov/pv/assets/pdfs/best-research-cell-efficiencies.20200925.pdf>.
- [7] M. Saliba, T. Matsui, J. Y. Seo, K. Domanski, J. P. Correa-Baena, M. K. Nazeeruddin, S. M. Zakeeruddin, W. Tress, A. Abate, A. Hagfeldt, M. Grätzel, *Energy Environ. Sci.* **2016**, *9*, 1989.
- [8] S. S. Mali, C. K. Hong, *Nanoscale* **2016**, *8*, 10528.
- [9] M. F. M. Noh, C. H. Teh, R. Daik, E. L. Lim, C. C. Yap, M. A. Ibrahim, N. A. Ludin, A. R. B. M. Yusoff, J. Jang, M. A. M. Teridi, *J. Mater. Chem. C* **2018**, *6*, 682.
- [10] B. Ding, S. Y. Huang, Q. Q. Chu, Y. Li, C. X. Li, C. J. Li, G. J. Yang, *J. Mater. Chem. A* **2018**, *6*, 10233.
- [11] A. K. Jena, A. Kulkarni, T. Miyasaka, *Chem. Rev.* **2019**, *119*, 3036.
- [12] F. Di Giacomo, A. Fakharuddin, R. Jose, T. M. Brown, *Energy Environ. Sci.* **2016**, *9*, 3007.
- [13] K. Mahmood, S. Sarwar, M. T. Mehran, *RSC Adv.* **2017**, *7*, 17044.
- [14] K. Choi, J. Lee, H. Il Kim, C. W. Park, G. W. Kim, H. Choi, S. Park, S. A. Park, T. Park, *Energy Environ. Sci.* **2018**, *11*, 3238.
- [15] P.-K. Kung, M.-H. Li, P.-Y. Lin, Y.-H. Chiang, C.-R. Chan, T.-F. Guo, P. Chen, *Adv. Mater. Interfaces* **2018**, *5*, 1800882.
- [16] N. E. Courtier, J. M. Cave, J. M. Foster, A. B. Walker, G. Richardson, *Energy Environ. Sci.* **2019**, *12*, 396.
- [17] P. Vivo, J. K. Salunke, A. Priimagi, *Materials* **2017**, *10*, 1087.
- [18] M. Jeong, I. W. Choi, E. M. Go, Y. Cho, M. Kim, B. Lee, S. Jeong, Y. Jo, H. W. Choi, J. Lee, J.-H. Bae, S. K. Kwak, D. S. Kim, C. Yang, *Science* **2020**, *369*, 1615.
- [19] L. Hu, M. Li, K. Yang, Z. Xiong, B. Yang, M. Wang, X. Tang, Z. Zang, X. Liu, B. Li, Z. Xiao, S. Lu, H. Gong, J. Ouyang, K. Sun, *J. Mater. Chem. A*, **2018**, *6*, 16583.
- [20] R. Singh, P. K. Singh, B. Bhattacharya, H.-W. Rhee, *Appl. Mater. Today* **2019**, *14*, 175.

- [21] P. Qin, S. Tanaka, S. Ito, N. Tetreault, K. Manabe, H. Nishino, M. K. Nazeeruddin, M. Grätzel, *Nat. Commun.* **2014**, *5*, 3834.
- [22] J. A. Christians, R. C. M. Fung, P. V. Kamat, *J. Am. Chem. Soc.*, **2014**, *136*, 758.
- [23] W. Yu, F. Li, H. Wang, E. Alarousu, Y. Chen, B. Lin, L. Wang, M. N. Hedhili, Y. Li, K. Wu, X. Wang, O. F. Mohammed, T. Wu, *Nanoscale* **2016**, *8*, 6173.
- [24] H. Rao, W. Sun, S. Ye, W. Yan, Y. Li, H. Peng, Z. Liu, Z. Bian, C. Huang, *ACS Appl. Mater. Interfaces* **2016**, *8*, 7800.
- [25] H. Zhang, H. Wang, W. Chen, A. K.-Y. Jen, *Adv. Mater.* **2017**, *29*, 1604984.
- [26] F. Igbari, M. Li, Y. Hu, Z. K. Wang, L. S. Liao, *J. Mater. Chem. A* **2016**, *4*, 1326.
- [27] Md. B. Islam, M. Yanagida, Y. Shirai, Y. Nabetani, K. Miyano, *ACS Omega* **2017**, *5*, 2291.
- [28] Z.-L. Tseng, L.-C. Chen, C.-H. Chiang, S.-H. Chang, C.-C. Chen, C.-G. Wu, *Sol. Energy* **2016**, *139*, 484.
- [29] M. Xiao, M. Gao, F. Huang, A. R. Pascoe, T. Qin, Y.-B. Cheng, U. Bach, L. Spiccia, *Chemnanomat* **2016**, *2*, 182.
- [30] U. Dasgupta, S. Chatterjee, A. J. Pal, *Sol. Energy Mater. Sol. Cells* **2017**, *172*, 353.
- [31] M. A. Wittenauer, L. L. Van Zandt, *Philos. Mag. B Phys. Condens. Matter; Stat. Mech. Electron. Opt. Magn. Prop.* **1982**, *46*, 659.
- [32] X. Yin, Y. Guo, H. Xie, W. Que, L. B. Kong, *Sol. RRL* **2019**, *3*, 1900001.
- [33] M. Martínez-Gil, M. I. Pintor-Monroy, M. Cota-Leal, D. Cabrera-German, A. Garzon-Fonoteca, M. A. Quevedo-López, M. Sotelo-Lerma, *Mater. Sci. Semicond. Process.* **2017**, *72*, 37.
- [34] F. Jiang, W. C. H. Choy, X. Li, D. Zhang, J. Cheng, *Adv. Mater.* **2015**, *27*, 2930.
- [35] D. Di Girolamo, F. Di Giacomo, F. Matteocci, A. G. Marrani, D. Dini, A. Abate, D. Di Girolamo, *Chem. Sci.* **2020**, *11*, 7746.
- [36] T. Abzieher, S. Moghadamzadeh, F. Schackmar, H. Eggers, F. Sutterlüti, A. Farooq, D. Kojda, K. Hbicht, R. Schmager, A. Mertens, R. Azmi, L. Kloth, J. A. Schwenzer, M. Hetterich, U. Lemmer, B. S. Richards, M. Powalla, U. W. Paetzold, *Adv. Energy Mater.* **2019**, *9*, 1802995.
- [37] U. Kwon, B. G. Kim, D. C. Nguyen, J. H. Park, N. Y. Ha, S. J. Kim, S. H. Ko, S. Lee, D. Lee, H. J. Park, *Sci. Rep.* **2016**, *6*, 32355.
- [38] L. Xu, X. Chen, J. Jin, W. Liu, B. Dong, X. Bai, H. Song, P. Reiss, *Nano Energy* **2019**, *63*, 103860.
- [39] S. Shao, M. A. Loi, *Adv. Mater. Interfaces* **2020**, *7*, 1901469.
- [40] H. S. Kim, C. R. Lee, J. H. Im, K. B. Lee, T. Moehl, A. Marchioro, S. J. Moon, R. Humphry-Baker, J. H. Yum, J. E. Moser, M. Grätzel, N. G. Park, *Sci. Rep.* **2012**, *2*, 591.
- [41] H. J. S. Michael, M. Lee, J. Teuscher, T. Miyasaka, T. N. Murakami, *Science* **2012**, *338*, 643.
- [42] D. Bi, S. J. Moon, L. Häggman, G. Boschloo, L. Yang, E. M. J. Johansson, M. K. Nazeeruddin, M. Grätzel, A. Hagfeldt, *RSC Adv.* **2013**, *3*, 18762.
- [43] M. Liu, M. B. Johnston, H. J. Snaith, *Nature* **2013**, *501*, 395.
- [44] W. Ke, G. Fang, J. Wan, H. Tao, Q. Liu, L. Xiong, P. Qin, J. Wang, H. Lei, G. Yang, M. Qin, X. Zhao, Y. Yan, *Nat. Commun.* **2015**, *6*, 6700.
- [45] Q. Hu, J. Wu, C. Jiang, T. Liu, X. Que, R. Zhu, Q. Gong, *ACS Nano* **2014**, *8*, 10161.
- [46] L. Etgar, P. Gao, Z. Xue, Q. Peng, A. K. Chandiran, B. Liu, M. K. Nazeeruddin, M. Grätzel, *J. Am. Chem. Soc.* **2012**, *134*, 17396.
- [47] I. Hotový, D. Búć, Š. Haščík, O. Nennowitz, *Vacuum* **1998**, *50*, 41.
- [48] J. Kim, H. J. Park, C. P. Grigoropoulos, D. Lee, J. Jang, *Nanoscale* **2016**, *8*, 17608.
- [49] X. Yin, J. Liu, J. Ma, C. Zhang, P. Chen, M. Que, Y. Yang, W. Que, C. Niu, J. Shao, *J. Power Sources* **2016**, *329*, 398.
- [50] J. Tang, D. Jiao, L. Zhang, X. Zhang, X. Xu, C. Yao, J. Wu, Z. Lan, *Sol. Energy* **2018**, *161*, 100.
- [51] X. Yin, P. Chen, M. Que, Y. Xing, W. Que, C. Niu, J. Shao, *ACS Nano* **2016**, *10*, 3630.
- [52] H. Zhang, J. Cheng, F. Lin, H. He, J. Mao, K. S. Wong, A. K. Y. Jen, W. C. H. Choy, *ACS Nano* **2016**, *10*, 1503.
- [53] J. Ciro, D. Ramírez, M. A. Mejía Escobar, J. F. Montoya, S. Mesa, R. Betancur, F. Jaramillo, *ACS Appl. Mater. Interfaces* **2017**, *9*, 12348.
- [54] M. Najafi, F. Di Giacomo, D. Zhang, S. Shanmugam, A. Senes, W. Verhees, A. Hadipour, Y. Galagan, T. Aernouts, S. Veenstra, R. Andriessen, *Small* **2018**, *14*, 1702775.
- [55] Z. Wang, X. Rong, L. Wang, W. Wang, H. Lin, X. Li, *ACS Appl. Mater. Interfaces* **2020**, *12*, 8342.
- [56] P. Ru, E. Bi, Y. Zhang, Y. Wang, W. Kong, Y. Sha, W. Tang, P. Zhang, Y. Wu, W. Chen, X. Yang, H. Chen, L. Han, *Adv. Energy Mater.* **2020**, *10*, 1903487.
- [57] J. He, E. Bi, W. Tang, Y. Wang, Z. Zhou, X. Yang, H. Chen, L. Han, *Sol. RRL* **2018**, *2*, 1800004.
- [58] X. Zhao, J. Chen, N. G. Park, *Sol. RRL* **2019**, *3*, 1800339.
- [59] J. You, L. Meng, T. Bin Song, T. F. Guo, W. H. Chang, Z. Hong, H. Chen, H. Zhou, Q. Chen, Y. Liu, N. De Marco, Y. Yang, *Nat. Nanotechnol.* **2016**, *11*, 75.
- [60] Y. Bai, H. Chen, S. Xiao, Q. Xue, T. Zhang, Z. Zhu, Q. Li, C. Hu, Y. Yang, Z. Hu, F. Huang, K. S. Wong, H. L. Yip, S. Yang, *Adv. Funct. Mater.* **2016**, *26*, 2950.
- [61] L. Hu, J. Peng, W. Wang, Z. Xia, J. Yuan, J. Lu, X. Huang, W. Ma, H. Song, W. Chen, Y. B. Cheng, J. Tang, *ACS Photonics* **2014**, *1*, 547.
- [62] J. Y. Jeng, K. C. Chen, T. Y. Chiang, P. Y. Lin, T. Da Tsai, Y. C. Chang, T. F. Guo, P. Chen, T. C. Wen, Y. J. Hsu, *Adv. Mater.* **2014**, *26*, 4107.
- [63] Y. Bai, H. Yu, Z. Zhu, K. Jiang, T. Zhang, N. Zhao, S. Yang, H. Yan, *J. Mater. Chem. A* **2015**, *3*, 9098.
- [64] X. Yin, Z. Yao, Q. Luo, X. Dai, Y. Zhou, Y. Zhang, Y. Zhou, S. Luo, J. Li, N. Wang, H. Lin, *ACS Appl. Mater. Interfaces* **2017**, *9*, 2439.
- [65] S. Xiao, Y. Bai, X. Meng, T. Zhang, H. Chen, X. Zheng, C. Hu, Y. Qu, S. Yang, *Adv. Funct. Mater.* **2017**, *27*, 1604944.
- [66] Z. Zhu, Y. Bai, X. Liu, C. C. Chueh, S. Yang, A. K. Y. Jen, *Adv. Mater.* **2016**, *28*, 6478.
- [67] G. A. Niklasson, C. G. Granqvist, *J. Mater. Chem.* **2007**, *17*, 127.
- [68] X. Yin, M. Que, Y. Xing, W. Que, *J. Mater. Chem. A* **2015**, *3*, 24495.
- [69] Y. Wu, F. Xie, H. Chen, X. Yang, H. Su, M. Cai, Z. Zhou, T. Noda, L. Han, *Adv. Mater.* **2017**, *29*, 1701073.
- [70] M. Yin, F. Xie, H. Chen, X. Yang, F. Ye, E. Bi, Y. Wu, M. Cai, L. Han, *J. Mater. Chem. A* **2016**, *4*, 8548.
- [71] F. Ye, H. Chen, F. Xie, W. Tang, M. Yin, J. He, E. Bi, Y. Wang, X. Yang, L. Han, *Energy Environ. Sci.* **2016**, *9*, 2295.
- [72] P. S. Patil, L. D. Kadam, *Appl. Surf. Sci.* **2002**, *199*, 211.
- [73] R. S. Kate, S. C. Bulakhe, R. J. Deokate, *J. Electron. Mater.* **2019**, *5*, 3220.
- [74] K. O. Ukoba, A. C. Eloka-Eboka, F. L. Inambao, *Renew. Sustain. Energy Rev.* **2018**, *82*, 2900.
- [75] J. W. Hennek, J. Smith, A. Yan, M. G. Kim, W. Zhao, V. P. Dravid, A. Facchetti, T. J. Marks, *J. Am. Chem. Soc.* **2013**, *135*, 10729.
- [76] A. Varma, A. S. Mukasyan, A. S. Rogachev, K. V. Manukyan, *Chem. Rev.* **2016**, *116*, 14493.
- [77] S. Bai, M. Cao, Y. Jin, X. Dai, X. Liang, Z. Ye, M. Li, J. Cheng, X. Xiao, Z. Wu, Z. Xia, B. Sun, E. Wang, Y. Mo, F. Gao, F. Zhang, *Adv. Energy Mater.* **2014**, *4*, 1301460.
- [78] J. W. Jung, C. C. Chueh, A. K. Y. Jen, *Adv. Mater.* **2015**, *27*, 7874.
- [79] Z. Liu, J. Chang, Z. Lin, L. Zhou, Z. Yang, D. Chen, C. Zhang, S. (Frank) Liu, Y. Hao, *Adv. Energy Mater.* **2018**, *8*, 1703432.
- [80] A. S. Subbiah, A. Halder, S. Ghosh, N. Mahuli, G. Hodes, S. K. Sarkar, *J. Phys. Chem. Lett.* **2014**, *5*, 1748.

- [81] I. J. Park, G. Kang, M. A. Park, J. S. Kim, S. W. Seo, D. H. Kim, K. Zhu, T. Park, J. Y. Kim, *ChemSusChem* **2017**, *10*, 2660.
- [82] J. H. Park, J. Seo, S. Park, S. S. Shin, Y. C. Kim, N. J. Jeon, H. W. Shin, T. K. Ahn, J. H. Noh, S. C. Yoon, C. S. Hwang, S. Il Seok, *Adv. Mater.* **2015**, *27*, 4013.
- [83] S. R. Pae, S. Byun, J. Kim, M. Kim, I. Gereige, B. Shin, *ACS Appl. Mater. Interfaces* **2018**, *10*, 534.
- [84] A. K. Mahmud Hassn, K. Sobayel, I. Raifuku, Y. Ishikawa, Md. Shahiduzzaman, M. Nour, H. Sindi, H. Moria, M. Rawa, K. Sopian, N. Amin, Md. Akhtaruzzaman, *Results Phys.* **2020**, *17*, 103122.
- [85] A. K. Mahmud Hasan, I. Raifuku, N. Amin, Y. Ishikawa, D. K. Sarkar, K. Sobayel, M. R. Karim, A. Ui-Hamid, H. Abdullah, Md. Shahiduzzaman, Y. Uraoka, K. Sopian, Md. Akhtaruzzaman, *Opt. Mater. Express* **2020**, *8*, 1801.
- [86] H. L. Chen, Y. M. Lu, W. S. Hwang, *Thin Solid Films* **2006**, *498*, 266.
- [87] Y. M. Lu, W. S. Hwang, J. S. Yang, H. C. Chuang, *Thin Solid Films* **2002**, *420–421*, 54.
- [88] G. Li, Y. Jiang, S. Deng, A. Tam, P. Xu, M. Wong, H. S. Kwok, *Adv. Sci.* **2017**, *4*, 1700463.
- [89] J. Cui, F. Meng, H. Zhang, K. Cao, H. Yuan, Y. Cheng, F. Huang, M. Wang, *ACS Appl. Mater. Interfaces* **2014**, *6*, 22862.
- [90] B. Abdollahi Nejand, V. Ahmadi, H. R. Shahverdi, *ACS Appl. Mater. Interfaces* **2015**, *7*, 21807.
- [91] M. Yanagida, L. Shimomoto, Y. Shirai, K. Miyano, *Electrochemistry* **2017**, *85*, 231.
- [92] K. C. Icli, M. Ozenbas, *Electrochim. Acta* **2018**, *263*, 338.
- [93] S. Seo, I. J. Par, M. Kim, S. Lee, C. Bae, H. S. Jung, N.-G. Park, J. Y. Kim, H. Shin, *Nanoscale*, **2016**, *8*, 11403.
- [94] X. Zheng, Y. Hou, C. Bao, J. Yin, F. Yuan, Z. Huang, K. Song, J. Liu, J. Troughton, N. Gasparini, C. Zhou, Y. Lin, D.-J. Xue, B. Chen, A. K. Johnston, N. Wei, M. N. Hedhili, M. Wei, A. Y. Alsalloum, P. Maity, B. Turedi, C. Yang, D. Baran, T. D. Anthopoulos, Y. Han, Z.-H. Lu, O. F. Mohammed, F. Gao, E. H. Sargent, O. M. Bakr, *Nat. Energy* **2020**, *5*, 131.
- [95] P. Gupta, T. Dutta, S. Mal, J. Narayan, *J. Appl. Phys.* **2012**, *111*, 013706.
- [96] P. H. Lee, B. T. Li, C. F. Lee, Z. H. Huang, Y. C. Huang, W. F. Su, *Sol. Energy Mater. Sol. Cells* **2020**, *208*, 110352.
- [97] M. Feng, M. Wang, H. Zhou, W. Li, S. Wang, Z. Zang, S. Chen, *ACS Appl. Mater. Interfaces* **2020**, *12*, 50684.
- [98] Y. Wei, K. Yao, X. Wang, Y. Jiang, X. Liu, N. Zhou, F. Li, *Appl. Surf. Sci.* **2018**, *427*, 782.
- [99] B. Parida, S. Yoon, J. Ryu, S. Hayase, S. M. Jeong, D. W. Kang, *ACS Appl. Mater. Interfaces* **2020**, *12*, 22958.
- [100] J. H. Lee, Y. W. Noh, I. S. Jin, J. W. Jung, *Electrochim. Acta* **2018**, *284*, 253.
- [101] P. S. Chandrasekhar, Y. H. Seo, Y. J. Noh, S. I. Na, *Appl. Surf. Sci.* **2019**, *481*, 588.
- [102] W. Chen, Y. Wu, J. Fan, A. B. Djurišić, F. Liu, H. W. Tam, A. Ng, C. Surya, W. K. Chan, D. Wang, Z. B. He, *Adv. Energy Mater.* **2018**, *8*, 1703519.
- [103] A. Bashir, L. J. Haur, S. Shukla, D. Gupta, T. Baikie, S. Chakraborty, R. Patidar, A. Bruno, S. Mhaisalkar, Z. Akhter, *Sol. Energy* **2019**, *182*, 225.
- [104] J. Kim, H. R. Lee, H. P. Kim, T. Lin, A. Kanwat, A. R. Bin Mohd Yusoff, J. Jang, *Nanoscale* **2016**, *8*, 9284.
- [105] S. Hietzschold, S. Hillebrandt, F. Ullrich, J. Bombsch, V. Rohnacher, S. Ma, W. Liu, A. Köhn, W. Jaegermann, A. Pucci, W. Kowalsky, E. Mankel, S. Beck, R. Lovrincic, *ACS Appl. Mater. Interfaces* **2017**, *9*, 39821.
- [106] J. Yang, K. M. Fransishyn, T. L. Kelly, *Chem. Mater.* **2016**, *28*, 7344.
- [107] J. He, Y. Xiang, F. Zhang, J. Lian, R. Hu, P. Zeng, J. Song, J. Qu, *Nano Energy* **2018**, *45*, 471.
- [108] A. B. Huang, J. T. Zhu, J. Y. Zheng, Y. Yu, Y. Liu, S. W. Yang, S. H. Bao, L. Lei, P. Jin, *J. Mater. Chem. C* **2016**, *4*, 10839.
- [109] Y. Xie, K. Lu, J. Duan, Y. Jiang, L. Hu, T. Liu, Y. Zhou, B. Hu, *ACS Appl. Mater. Interfaces* **2018**, *10*, 14153.
- [110] J. H. Lee, Y. W. Noh, I. S. Jin, S. H. Park, J. W. Jung, *J. Power Sources* **2019**, *412*, 425.
- [111] Y. Ashok Kumar Reddy, A. Sivasankar Reddy, P. Sreedhara Reddy, *J. Alloys Compd.* **2014**, *583*, 396.
- [112] J. Zheng, L. Hu, J. S. Yun, M. Zhang, C. F. J. Lau, J. Bing, X. Deng, Q. Ma, Y. Cho, W. Fu, C. Chen, M. A. Green, S. Huang, A. W. Y. Ho-Baillie, *ACS Appl. Energy Mater.* **2018**, *1*, 561.
- [113] M. A. Hameed, O. A. Ali, S. S. M. Al-Awadi, *Optik* **2020**, *206*, 164352.
- [114] J. A. Flores-Livas, R. Sarmiento-Pérez, S. Botti, S. Goedecker, M. A. L. Marques, *J. Phys. Mater.* **2019**, *2*, 025003.
- [115] H. Yavas, M. Sundermann, K. Chen, A. Amorese, A. Severing, H. Gretarsson, M. W. Haverkort, L. H. Tjeng, *Nat. Phys.* **2019**, *15*, 559.
- [116] A. R. Puigdollers, P. Schlexer, S. Tosoni, G. Pacchioni, *ACS Catal.* **2017**, *7*, 6493.
- [117] X. Chen, L. Xu, C. Chen, Y. Wu, W. Bi, Z. Song, X. Zhuang, S. Yang, S. Zhu, H. Song, *J. Power Sources* **2019**, *444*, 227267.
- [118] S. Goumri-Said, W. Khan, K. Boubaker, G. Turgut, E. Sönmez, J. Minar, M. Bououdina, M. B. Kanoun, *Mater. Res. Bull.* **2019**, *118*, 110525.
- [119] Z. Hu, D. Chen, P. Yang, L. Yang, L. Qin, Y. Huang, X. Zhao, *Appl. Surf. Sci.* **2018**, *441*, 258.
- [120] S. Teo, Z. Guo, Z. Xu, C. Zhang, Y. Kamata, S. Hayase, T. Ma, *ChemSusChem* **2019**, *12*, 518.
- [121] S. C. Chen, T. Y. Kuo, Y. C. Lin, H. C. Lin, *Thin Solid Films* **2011**, *519*, 4944.
- [122] K. H. Kim, C. Takahashi, Y. Abe, M. Kawamura, *Optik* **2014**, *125*, 2899.
- [123] F. Ma, Y. Zhao, J. Li, X. Zhang, H. Gu, J. You, *J. Energy Chem.* **2020**, *52*, 393.
- [124] W. Chen, Y. Wu, Y. Yue, J. Liu, W. Zhang, X. Yang, H. Chen, E. Bi, I. Ashraf, M. Grätzel, L. Han, *Science* **2015**, *350*, 944.
- [125] X. Xia, Y. Jiang, Q. Wan, X. Wang, L. Wang, F. Li, *ACS Appl. Mater. Interfaces* **2018**, *10*, 44501.
- [126] G. Niu, S. Wang, J. Li, W. Li, L. Wang, *J. Mater. Chem. A* **2018**, *6*, 4721.
- [127] M.-H. Liu, Z.-J. Zhou, P.-P. Zhang, Q.-W. Tian, W.-H. Zhou, D.-X. Kou, S.-X. Wu, *Opt. Express* **2016**, *24*, A1349.
- [128] S. Wang, B. Zhang, D. Feng, Z. Lin, J. Zhang, Y. Hao, X. Fan, J. Chang, *J. Mater. Chem. C* **2019**, *7*, 9270.
- [129] D. Hou, J. Zhang, X. Gan, H. Yuan, L. Yu, C. Lu, H. Sun, Z. Hu, Y. Zhu, *J. Colloid Interface Sci.* **2020**, *559*, 29.
- [130] R. Islam, G. Chen, P. Ramesh, J. Suh, N. Fuchigami, D. Lee, K. A. Littau, K. Weiner, R. T. Collins, K. C. Saraswat, *ACS Appl. Mater. Interfaces* **2017**, *9*, 17201.
- [131] F. Gao, Y. Zhao, X. Zhang, J. You, *Adv. Energy Mater.* **2020**, *10*, 1902650.
- [132] W. Chen, Y. Zhou, L. Wang, Y. Wu, B. Tu, B. Yu, F. Liu, H. W. Tam, G. Wang, A. B. Djurišić, L. Huang, Z. He, *Adv. Mater.* **2018**, *30*, 180015.
- [133] Y. Cheng, M. Li, X. Liu, S. H. Cheung, H. T. Chandran, H. W. Li, X. Xu, Y. M. Xie, S. K. So, H. L. Yip, S. W. Tsang, *Nano Energy* **2019**, *61*, 496.
- [134] J. Zhang, H. Luo, W. Xie, X. Lin, X. Hou, J. Zhou, S. Huang, W. Ou-Yang, Z. Sun, X. Chen, *Nanoscale* **2018**, *10*, 5617.

- [135] Y. Du, C. Xin, W. Huang, B. Shi, Y. Ding, C. Wei, Y. Zhao, Y. Li, X. Zhang, *ACS Sustain. Chem. Eng.* **2018**, *6*, 16806.
- [136] D. Di Girolamo, N. Phung, M. Jošt, A. Al-Ashouri, G. Chistiakova, J. Li, J. A. Márquez, T. Unold, L. Korte, S. Albrecht, A. Di Carlo, D. Dini, A. Abate, *Adv. Mater. Interfaces* **2019**, *6*, 1900789.
- [137] W. Chen, Y. Zhou, G. Chen, Y. Wu, B. Tu, F. Z. Liu, L. Huang, A. M. C. Ng, A. B. Djurišić, Z. He, *Adv. Energy Mater.* **2019**, *9*, 1803872.
- [138] Q. Xue, Y. Bai, M. Liu, R. Xia, Z. Hu, Z. Chen, X. F. Jiang, F. Huang, S. Yang, Y. Matsuo, H. L. Yip, Y. Cao, *Adv. Energy Mater.* **2017**, *7*, 1602333.
- [139] J. Zhao, R. Tavakoli, M. M. Tavakoli, *Chem. Commun.* **2019**, *55*, 9196.
- [140] Z. Li, B. H. Jo, S. J. Hwang, T. H. Kim, S. Somasundaram, E. Kamaraj, J. Bang, T. K. Ahn, S. Park, H. J. Park, *Adv. Sci.* **2019**, *6*, 1802163.
- [141] A. Jäger-Waldau, P. V. Status Report 2018, https://ec.europa.eu/jrc/sites/jrcsh/files/pv_status_report_2018_online.pdf (accessed: March 2018).
- [142] N. N. Lal, Y. Dkhissi, W. Li, Q. Hou, Y.-B. Cheng, U. Bach, *Adv. Energy Mater.* **2017**, *7*, 1602761.
- [143] Z. J. Yu, J. V. Carpenter III, Z. C. Holman, *Nat. Energy* **2018**, *3*, 747.
- [144] W. Travis, E. N. K. Glover, H. Bronstein, D. O. Scanlon, R. G. Palgrave, *Chem. Sci.* **2016**, *7*, 4548.
- [145] J. Tong, Z. Song, D. H. Kim, X. Chen, C. Chen, A. F. Palmstrom, P. F. Ndione, M. O. Reese, S. P. Dunfield, O. G. Reid, J. Liu, F. Zhang, S. P. Harvey, Z. Li, S. T. Christensen, G. Teeter, D. Zhao, M. M. Al-Jassim, M. F. A. M. van Hest, M. C. Beard, S. E. Shaheen, J. J. Berry, Y. Yan, K. Zhu, *Science* **2019**, *364*, 475.
- [146] N.-G. Park, *Mater. Today* **2015**, *18*, 65.
- [147] T. S. Liang, M. Pravettoni, C. Deline, J. S. Stein, R. Kopecek, J. P. Singh, W. Luo, Y. Wang, A. G. Aberle, Y. S. Khoo, *Energy Environ. Sci.* **2019**, *12*, 116.
- [148] J. Ramanujam, U. P. Singh, *Energy Environ. Sci.* **2017**, *10*, 1306.
- [149] Z. Li, T. H. Kim, S. Y. Han, Y.-J. Yun, S. Jeong, B. Jo, S. A. Ok, W. Yim, S. H. Lee, K. Kim, S. Moon, J.-Y. Park, T. K. Ahn, H. Shin, J. Lee, H. J. Park, *Adv. Energy Mater.* **2020**, *10*, 1903085.
- [150] I. S. E. Fraunhofer, Photovoltaics Report 2020, <https://www.ise.fraunhofer.de/content/dam/ise/de/documents/publications/studies/Photovoltaics-Report.pdf> (accessed: September 2020).
- [151] Z. Yu, M. Leilaoui, Z. Holman, *Nat. Energy* **2016**, *1*, 16137.
- [152] K. Yoshikawa, H. Kawasaki, W. Yoshida, T. Irie, K. Konishi, K. Nakano, T. Uto, D. Adachi, M. Kanematsu, H. Uzu, K. Yamamoto, *Nat. Energy* **2017**, *2*, 17032.
- [153] J. Xu, C. C. Boyd, Z. J. Yu, A. F. Palmstrom, D. J. Witter, B. W. Larson, R. M. France, J. Werner, S. P. Harvey, E. J. Wolf, W. Weigand, S. Manzoor, M. F. A. M. van Hest, J. J. Berry, J. M. Luther, Z. C. Holman, M. D. McGehee, *Science* **2020**, *367*, 1097.
- [154] A. Polman, M. Knight, E. C. Garnett, B. Ehrler, W. C. Sinke, *Science* **2016**, *352*, 307.
- [155] H. Li, W. Zhang, *Chem. Rev.* **2020**, *120*, 9835.
- [156] AAAS, World Record: Efficiency of Perovskite Silicon Tandem Solar Cell Jumps to 29.15%, **2020**. https://www.eurekalert.org/pub_releases/2020-01/hbfn-wre012920.php.
- [157] J. Werner, F. Sahli, F. Fu, J. J. D. Leon, A. Walter, B. A. Kamino, B. Niesen, S. Nicolay, Q. Jeangros, C. Ballif, *ACS Energy Lett.* **2018**, *3*, 2052.
- [158] A. Morales-Acevedo, *Energy Proc.* **2010**, *2*, 169.
- [159] Solar Frontier, Solar Frontier Achieves World Record Thin-Film Solar Cell Efficiency of 23.35%, **2019**, http://www.solar-frontier.com/eng/news/2019/0117_press.html (accessed: January 2019).
- [160] F. Fu, T. Feurer, T. Jäger, E. Avncini, B. Bissig, S. Yoon, S. Buecheler, A. N. Tiwari, *Nat. Commun.* **2015**, *6*, 8932.
- [161] C. D. Bailie, M. G. Christoforo, J. P. Mailoa, A. R. Bowring, E. L. Unger, W. H. Nguyen, J. Burschka, N. Pellet, J. Z. Lee, M. Grätzel, R. Noufi, T. Buonassisi, A. Salleo, M. D. McGehee, *Energy Environ. Sci.* **2015**, *8*, 956.
- [162] M. Jošt, T. Bertram, D. Koushik, J. A. Marquez, M. A. Verheijen, M. D. Heinemann, E. Köhnen, A. Al-Ashouri, S. Braunger, F. Lang, B. Rech, T. Unold, M. Creatore, I. Laueremann, C. A. Kaufmann, R. Schlattmann, S. Albrecht, *ACS Energy Lett.* **2019**, *4*, 583.
- [163] M. A. Green, K. Emery, Y. Hishikawa, W. Warta, E. D. Dunlop, D. H. Levi, A. W. Y. Ho-Baillie, *Prog. Photovoltaics* **2019**, *27*, 3.
- [164] P. Bhattacharya, R. Fornari, H. Kamimura, *Comprehensive Semiconductor Science and Technology* (Ed: R. Fornari), Vol. 3, Elsevier, Amsterdam **2011**.
- [165] L. L. Yan, C. Han, B. Shi, Y. Zhao, X. D. Zhang, *Mater. Today Nano* **2019**, *7*, 100045.
- [166] G. E. Eperon, M. T. Hörantner, H. J. Snaith, *Nat. Rev. Chem.* **2017**, *1*, 0095.
- [167] T. Leijtens, K. A. Bush, R. Prasanna, M. D. McGehee, *Nat. Energy* **2018**, *3*, 828.
- [168] K. Xiao, J. Wen, Q. Han, R. Lin, Y. Gao, S. Gu, Y. Zang, Y. Nie, J. Zhu, J. Xu, H. Tan, *ACS Energy Lett.* **2020**, *5*, 2819.
- [169] K. Xiao, R. Lin, Q. Han, Y. Hou, Z. Qin, H. T. Nguyen, J. Wen, M. Wei, V. Yeddu, M. I. Saidaminov, Y. Gao, X. Luo, Y. Wang, H. Gao, C. Zhang, J. Xu, J. Zhu, E. H. Sargent, H. Tan, *Nat. Energy* **2020**, *5*, 870.
- [170] F. Khan, B. D. Rezugui, J. H. Kim, *Sol. Energy* **2020**, *209*, 226.
- [171] X. Wan, Y. Jiang, Z. Qiu, H. Zhang, X. Zhu, I. Sikandar, X. Liu, X. Chen, B. Cao, *ACS Appl. Energy Mater.* **2018**, *1*, 3947.
- [172] A. Huang, L. Lei, Y. Chen, Y. Yu, Y. Zhou, Y. Liu, S. Yang, S. Bao, R. Li, P. Jin, *Sol. Energy Mater. Sol. Cells* **2018**, *182*, 128.
- [173] K. Yao, F. Li, Q. He, X. Wang, Y. Jiang, H. Huang, A. K. Y. Jen, *Nano Energy* **2017**, *40*, 155.
- [174] Q. He, K. Yao, X. Wang, X. Xia, S. Leng, F. Li, *ACS Appl. Mater. Inter.* **2017**, *9*, 41887.
- [175] S. Yue, K. Liu, R. Xu, M. Li, M. Azam, K. Ren, J. Liu, Y. Sun, Z. Wang, D. Cao, X. Yan, S. Qu, Y. Lei, Z. Wang, *Energy Environ. Sci.* **2017**, *10*, 2570.
- [176] D. C. Nguyen, S.-Y. Joe, N. Y. Ha, H. J. Park, J.-Y. Park, Y. H. Ahn, S. Lee, *Phys. Status Solidi R* **2017**, *11*, 1600395.
- [177] J. H. Kim, P. W. Liang, S. T. Williams, N. Cho, C. C. Chueh, M. S. Glaz, D. S. Ginger, A. K. Y. Jen, *Adv. Mater.* **2015**, *27*, 695.
- [178] Z. Saki, K. Sveinbjörnsson, G. Boschloo, N. Taghavinia, *ChemPhysChem* **2019**, *20*, 3322.
- [179] P. C. Chen, S. H. Yang, *ACS Appl. Energy Mater.* **2019**, *2*, 6705.
- [180] Q. Fu, S. Xiao, X. Tang, T. Hu, *Org. Electron.* **2019**, *69*, 34.
- [181] B. Ge, H. W. Qiao, Z. Q. Lin, Z. R. Zhou, A. P. Chen, S. Yang, Y. Hou, H. G. Yang, *Sol. RRL* **2019**, *3*, 1900192.
- [182] J. Zhang, W. Mao, X. Hou, J. Duan, J. Zhou, S. Huang, W. Ou-Yang, X. Zhang, Z. Sun, X. Chen, *Sol. Energy* **2018**, *174*, 1133.
- [183] M. A. Park, I. J. Park, S. Park, J. Kim, W. Jo, H. J. Son, J. Y. Kim, *Curr. Appl. Phys.* **2018**, *18*, S55.
- [184] W. Nie, H. Tsai, J.-C. Blancon, F. Liu, C. C. Stoumpos, B. Traore, M. Kepenekian, O. Durand, C. Katan, S. Tretiak, J. Rochet, P. M. Ajayan, M. G. Kanatzidis, J. Even, A. D. Mohite, *Adv. Mater.* **2018**, *30*, 1703879.
- [185] Z. Qiu, H. Gong, G. Zheng, S. Yuan, H. Zhang, X. Zhu, H. Zhou, B. Cao, *J. Mater. Chem. C* **2017**, *5*, 7084.
- [186] H.-S. Kim, J.-Y. Seo, H. Xie, M. Lira-Cantu, S. M. Zakeeruddin, M. Grätzel, A. Hagfeldt, *ACS Omega* **2017**, *2*, 9074.
- [187] Y. Wu, X. Yang, W. Chen, Y. Yue, M. Cai, F. Xie, E. Bi, A. Islam, L. Han, *Nat. Energy* **2016**, *1*, 16148.
- [188] S. Liu, S. Ho, Y. Chen, F. So, *Chem. Mater.* **2015**, *27*, 2532.

- [189] Q. Wang, C. C. Chueh, T. Zhao, J. Cheng, M. Eslamian, W. C. H. Choy, A. K. Y. Jen, *ChemSusChem* **2017**, *10*, 3794.
- [190] J. W. Jo, M. S. Seo, J. W. Jung, J. S. Park, B. H. Sohn, M. J. Ko, H. J. Son, *J. Power Sources* **2018**, *378*, 98.
- [191] J. H. Lee, Y. W. Noh, I. S. Jin, S. H. Park, J. W. Jung, *ACS Sustain. Chem. Eng.* **2019**, *7*, 15495.
- [192] B. Zhang, J. Su, X. Guo, L. Zhou, Z. Lin, L. Feng, J. Zhang, J. Chang, Y. Hao, *Adv. Sci.* **2020**, *7*, 1903044.
- [193] H. Anizelli, T. W. David, P. Tyagi, E. Laureto, J. Kettle, *Sol. Energy* **2020**, *203*, 157.
- [194] L. Xie, Z. Cao, J. Wang, A. Wang, S. Wang, Y. Cui, Y. Xiang, X. Niu, F. Hao, L. Ding, *Nano Energy* **2020**, *74*, 104846.
- [195] B. Jo, H. Park, E. Kamaraj, S. Lee, B. Jung, S. Somasundaram, G. G. Jeon, K. T. Lee, N. Kim, J. H. Kim, B. G. Kim, T. K. Ahn, S. Park, H. J. Park, *Adv. Funct. Mater.* **2020**, *31*, 2007180.



Hansol Park received his B.S. in organic and nano engineering from Hanyang University, Seoul, Korea. Currently, he is a Ph.D. candidate in Human-Tech Convergence Program at Hanyang University. His research interests are optoelectronics including inverted-type perovskite solar cells and perovskite tandem solar cells.



Hui Joon Park received his B.S. and M.S. in materials science and engineering from Seoul National University, Korea, in 2002 and 2004, respectively. From 2004 to 2007, he was with LG Electronics and Korea Institute of Science and Technology, Korea, as a researcher. He received a Ph.D. from University of Michigan, Ann Arbor, USA, in 2012. After his Ph.D., he became a senior researcher at Intel Corporation, USA, from 2012 to 2014. From 2014 to 2019, he was a faculty in Electrical and Computer Engineering at Ajou University, Korea. In 2019, he joined Hanyang University, Korea, where he is currently an associate professor.